Atmospheric Research 329 (2026) 108495

Contents lists available at ScienceDirect

Atmospheric Research

journal homepage: www.elsevier.com/locate/atmosres

Response of tropical cyclones to global warming: Super Typhoon Usagi in the Western Pacific Ocean

Qi Sun [a,b,*], Joël Arnault [a,b], Christopher Holst [a], Patrick Laux [a,b], Harald Kunstmann [a,b,c]

[a] Institute of Meteorology and Climate Research, Karlsruhe Institute of Technology, Garmisch-Partenkirchen, Germany
[b] Institute of Geography, University of Augsburg, Augsburg, Germany
[c] Centre for Climate Resilience, University of Augsburg, Augsburg, Germany

ARTICLE INFO

Keywords:
Climate change
Tropical cyclones
Extreme rainfall
Pseudo global warming approach

ABSTRACT

Climate change has the potential to significantly alter the characteristics of tropical cyclones (TCs). Understanding how representative extreme TCs with distinct meteorological structures and hydrological impacts respond to warming is critical for improving risk assessment. Super Typhoon Usagi (2013) represents a rare case, maintaining unusually high intensity at landfall while coinciding with an astronomical high tide—a combination infrequently observed in the climatological record—which led to severe compound flooding in coastal cities. However, how such exceptional TC characteristics respond to climate change remains unclear. In this study, we apply a high-resolution (5 km) Weather Research and Forecasting (WRF) model simulation within the Pseudo-Global Warming (PGW) framework, in which reanalysis-based initial and boundary conditions are perturbed by multi-variable warming signals from CMIP6 GCMs, to assess how climate change may alter the characteristics of Super Typhoon Usagi (2013). Our results indicate that the accumulated precipitation increases by up to 100 mm under future warming scenarios, along with an increase in peak intensity, range from 5 hPa (LESS_WARM) to 10 hPa (MORE_WARM)). Hourly precipitation is projected to rise by 6.5 %–26.4 %, exceed the temperature-induced CC scaling (4.2 %–20.3 %). Increased latent heat flux (30–90 W m^{-2}) under warmer (0.6–2.9 K) and wetter (1.5–4.0 g kg^{-1}) climate conditions enhances TC intensification. Warming also affects the dynamic structure of TCs, enhancing vertical velocity (2–4 Pa s^{-1}) and tangential wind (5–10 m s^{-1}), expanding the inflow and outflow regions contributing to a stronger TC. The unexpected increase in precipitation is driven by both thermodynamic and dynamic factors. This case study provides insights into the potential responses of landfalling TCs—particularly those linked to compound flooding—in the Western Pacific Ocean (WNP) under future climate change.

1. Introduction

Tropical cyclones (TCs) pose significant threats to coastal regions with extreme precipitation, strong wind, and associated storm surges, particularly in the most prosperous and densely populated economic areas along the China's southern coast (Shi et al., 2024; Chen et al., 2020). For example, Super Typhoon Usagi (2013) resulted in widespread flooding, transportation disruptions, and severe property damage (HKO, 2013). Climate change has been shown to profoundly affected TC characteristics, including their intensity, frequency and track (Seneviratne et al., 2021; Knutson et al., 2020, 2021). Notably, the projections indicate that the proportion of Category 4–5 TCs (Saffir-Simpson scale, Simpson and Saffir, 1974) will very likely increase globally (Knutson et al., 2020; Seneviratne et al., 2021). Besides, recent study (Wang and Toumi, 2022) show that the number of annual global TC landfalls with major landfall intensity has nearly doubled from 1982 to 2020. Therefore, investigating the response of climate change to severe landfall TC is of critical importance for public safety and coastal resilience.

Considerable progress has been achieved in recent decades toward the projections of TC characteristics under warming climate. General Circulation Models (GCMs) from the Coupled Model Intercomparison Project Phases 5 and 6 (CMIP5/6) are commonly used to study the TC response to climate change (Cha et al., 2020; Knutson et al., 2020). However, their coarse horizontal resolution (around 100–200 km grid spacing) cannot simulate TCs of Category 4–5 (Knutson et al., 2020;

* Corresponding author at: Institute of Meteorology and Climate Research, Karlsruhe Institute of Technology, Garmisch-Partenkirchen, Germany.
E-mail address: qi.sun@kit.edu (Q. Sun).

https://doi.org/10.1016/j.atmosres.2025.108495
Received 18 April 2025; Received in revised form 19 September 2025; Accepted 20 September 2025
Available online 2 October 2025

Seneviratne et al., 2021). High-resolution GCMs (around 10–100 km) have improvements but are computationally demanding (Manganello et al., 2014; Murakami et al., 2015; Roberts et al., 2018; Moon et al., 2022). To address the unrealistic TC structures caused by coarse spatial resolution and to reduce computational costs, downscaling methods are widely adopted, primarily falling into two categories: statistical (Pierce and Cayan, 2016; Jiang et al., 2018) and dynamical downscaling (Chih et al., 2022, 2024; Barcikowska et al., 2017; Emanuel, 2021; Knutson et al., 2022; Rendfrey et al., 2021; Pérez-Alarcón et al., 2024). Statistical downscaling, while computationally efficient and suitable for large GCM ensembles, relies on stationary empirical relationships and long-term observations, and may lack physical consistency across variables (Jones et al., 2023). As for dynamical downscaling, the regional climate models (RCMs) with horizontal of 1–10 km resolution can more precisely simulate TC eye-wall structures (Tsuboki et al., 2015; Lynn et al., 2009). However, they require additional lateral and surface boundary inputs. Nonetheless, RCMs are computationally expensive, and may inherit biases from the driving GCMs (Jones et al., 2023).

Thus, to overcome these limitations, the Pseudo Global Warming (PGW) approach (Schär et al., 1996; Kimura and Kitoh, 2007; Sato et al., 2007) has been widely adopted to asses the impacts of climate change on extreme events, including droughts, floods, extreme precipitation, heat waves, and TCs (Xue and Ullrich, 2021, 2022; Doan et al., 2022; Chan et al., 2023; Dougherty et al., 2023; Bercos-Hickey et al., 2022; Delfino et al., 2023; Hiraga et al., 2025). The method uses initial and boundary conditions derived from reanalysis data, which are perturbed by warming signals estimated from various coarse resolution GCM variables, to drive RCMs (1–10-km grid spacing), and asses how identical events might evolve under a warmer climate (Kimura and Kitoh, 2007; Sato et al., 2007). Compared to traditional direct downscaling, the PGW method can avoid the systematic biases in GCM boundary conditions, avoiding incorrect feedback passed to RCMs, and thus potentially improving our understanding of regional climate change processes (Adachi and Tomita, 2020) and impact assessments (Laux et al., 2021). Furthermore, the PGW method offers significant computational advantages, as it enables storyline-based downscaling of individual extreme events, rather than requiring long-term climate simulations. Numerous studies have applied the PGW method with projections to investigate response of TCs, including the Atlantic Ocean, Pacific Ocean, Australia, and the Bay of Bengal (Lynn et al., 2009; Lackmann, 2015; Nakamura et al., 2016; Parker et al., 2018; Patricola and Wehner, 2018; Gutmann et al., 2018; Mittal et al., 2019; Chen et al., 2020, 2022; Tran et al., 2022; Delfino et al., 2023). For example, in the Western North Pacific (WNP) basin, Chen et al. (2020) applied the PGW approach to landfalling TCs (Victor 1997, Utor 2001, Hagupit 2008) and found that peak TC intensities are projected to increase by approximately 10 % in the late 21st century under the RCP8.5 scenario. In a subsequent study, Chen et al. (2022) extended the analysis to 20 TC cases in the WNP and reported an average increase in peak intensity of 9 % ± 8 % under the same scenario. Similarly, Tran et al. (2022) employed PGW simulations using CMIP6 outputs under SSP3–7.0 scenarios, finding that the peak intensity of TCs could increase by approximately 9.25 hPa (1 %) by the 2090s. Delfino et al. (2023) also applied the PGW method to simulate three high-impact TCs (Haiyan 2013, Bopha 2012, Mangkhut 2018) using 5 km grid spacing WRF model, and found projected increases in maximum wind speeds of 4 %, 3 %, and 14 %, respectively, under the SSP5–8.5 scenario. Given the differences in TC intensity changes observed in previous studies across cases, it is essential to examine the potential response of TC characteristics to climate change in the WNP basin, particularly for landfalling TCs along southern coastal regions of China, a region highly vulnerable to TC impacts due to its dense population and complex coastal environment.

Super Typhoon Usagi (2013), a Category 4 TC (Simpson and Saffir, 1974), was one of the most intense and damaging TC to make landfall in eastern Guangdong Province (China's southern coast) over the past four decades, resulting in 35 fatalities and direct economic losses exceeding 20.8 billion RMB (CWN, 2013). Unlike many previously analyzed typhoons (e.g., Mangkhut 2018), Usagi's damage was not only due to strong winds or heavy rainfall, but also the result of compound flooding, caused by the simultaneous occurrence of astronomical high tide, heavy rainfall, and storm surge. This overlap of meteorological and tidal drivers resulted in widespread coastal inundation (HKO, 2013). Usagi thus represents a valuable case of a compound flood event (Sebastian, 2022) for understanding the atmospheric changes underlying such events, especially in the context of future climate change. To our knowledge, this study is among the first to focus on comprehensively analyze a compound-flood-inducing Typhoon Usagi, using the PGW framework. By exploring the underlying physical mechanisms driving these changes, this work provides novel insights into how such TCs may respond to a warming climate, thereby informing disaster risk management for similar events.

The performance of the PGW method in projecting TC changes is influenced by multiple factors. First, uncertainties arise from the warming signals used to perturb the initial and boundary conditions derived from global climate models (GCMs), such as those from CMIP5 and CMIP6. Accurate sea surface temperature (SST) representation is crucial for accurate projections of future TC (Seneviratne et al., 2021). Compared to CMIP5, CMIP6 reduces SST cooling biases over the WNP by 20 % (Zhang et al., 2023) and better captures thermodynamic conditions along the tracks of TCs affecting South Korea (Park et al., 2021). Since 2021, PGW studies in the WNP increasingly use CMIP6 outputs for TC projections (Chen et al., 2022; Tran et al., 2022; Delfino et al., 2023), likely due to their improved performance in simulating historical SSTs over the WNP, which increase confidence in future projections (Seneviratne et al., 2021). For example, Chen et al. (2022) applied the PGW method using the WRF model to downscale TCs based on both CMIP5 and CMIP6 outputs. Their results showed that the change in the radius of maximum wind (RMW) was more pronounced in the CMIP6 simulations (−10 % ± 5 %) compared to CMIP5, indicating a tendency toward more compact TCs.

Secondly, the selection of specific GCMs, emission scenarios, and consideration of internal climate variability to compute the climate change signal also affects the results of TC projections. Structural uncertainty from model selection is the dominant contributor among various sources of uncertainty in TC projections (Meiler et al., 2023). Previous studies have commonly adopted the Multi-Model Ensemble (MME) approach to combine outputs from multiple GCMs (Chen et al., 2022; Tran et al., 2022; Lin et al., 2024). However, this approach can result in biases toward the largest set of similar models and an underestimation of the inter-model uncertainty (Pathak et al., 2023). Additionally, the MME method can smooth out structural uncertainties and overlook the different physical process assumptions associated with different models (Mittal et al., 2019; Pathak et al., 2023). Therefore, selecting or classifying climate models based on their equilibrium climate sensitivity (ECS) has been increasingly adopted as an approach for exploring model uncertainty (Delfino et al., 2023; Jones et al., 2023). For example, Jones et al. (2023) grouped global climate models into high- and low- climate sensitivity categories based on ECS to examine how different warming responses influence projections. Delfino et al. (2023) selected four GCMs based on ECS for PGW downscaling to investigate the sensitivity of TC intensity, track, and translation speed to warming signals from different GCMs, but did not examine changes in precipitation. Tahara et al. (2025) considered the uncertainties in projecting extreme Mesoscale Convective Systems-related precipitation using three GCMs. However, few studies have examined the sensitivity of TC precipitation projections to the choice of GCMs based on ECS, especially using CMIP6 datasets.

Lastly, the choice of perturbation variables within the PGW framework also play a critical role in shaping the simulated TC characteristics. Some studies only perturbed both thermodynamic variables. For example, Yang and Toumi (2025) considered only SSTs in their projections. Lee et al. (2023) considered the SST, atmospheric temperature

(Ta), and relative humidity (RH) in the projections. Tran et al. (2022) highlighted the necessity of perturbing both thermodynamic and dynamic variables (SST, Ta, RH, and winds), which is particularly crucial for short-term simulations. Brogli et al. (2023) emphasized the importance of adjusting the pressure and geopotential height fields to ensure consistency between thermodynamic and dynamic changes. However, only few studies have taken such adjustments into consideration in TC downscaling with PGW method.

Most PGW downscaling studies consistently suggest that TCs in the WNP are projected to intensify (Tran et al., 2022; Chen et al., 2022; Delfino et al., 2023) and produce more precipitation (Tran et al., 2022; Chen et al., 2022), while changes in translation speed, track, and TC size remain relatively small (Tran et al., 2022; Delfino et al., 2023). Despite the general agreement on increased TC-induced rainfall, discrepancies arise when examining the radial structure of precipitation and the magnitude of rainfall rate increases. Satellite-based observations indicate a decreasing trend in inner-core rainfall rates, accompanied by enhanced rainfall in the outer regions of TCs (Guzman and Jiang, 2021; Wei et al., 2022). In contrast, most modeling studies (Liu et al., 2019; Patricola and Wehner, 2018; Tran et al., 2024) project a pronounced increase in inner-core rainfall. Understanding the spatial distribution and quantitative changes of TC rainfall is critical for effective coastal disaster management. Additionally, the relative contributions of dynamic and thermodynamic factors to changes of TC rainfall under future warming remains unclear.

The key innovations of this study are as follows: (1) We focus on a unique and understudied case—Super Typhoon Usagi (2013)—which was associated with a significant compound flooding event. (2) We employ a modeling framework that combines dynamical downscaling using the high-resolution (5 km) WRF model with PGW approach, forced by both high- and low-climate-sensitivity GCMs from CMIP6. Importantly, perturbing key oceanic and atmospheric variables (SST, Ta, RH, winds) and adjusting pressure and geopotential height for consistency. (3) We examine the projected changes in the inner-core of TC rainfall and assess the relative contributions of dynamic and thermodynamic factors to TC rainfall.

Above all, this study aims to investigate the impact of global warming on a Super Typhoon event in the WNP, which is known to trigger coastal compound flood event—an increasingly critical phenomenon with significant implications for both regional infrastructure and disaster preparedness. In this study, we specifically address the following research questions: (1) How do the intensity of Super Typhoon Usagi (2013), respond to global warming under the SSP5–8.5 scenario? (2) To what extent will global warming alter precipitation rates in Super Typhoon Usagi (2013), and how do these changes compare with the theoretical scaling of precipitation with temperature (Clausius–Clapeyron relation)? (3) What are the relative contributions of thermodynamic and dynamic factors to the projected changes in precipitation, considering sensitivities to high- and low- climate sensitivity GCMs from CMIP6?

The rest of the article is organized as follows: Section. 2 presents a brief overview of the TC case, the experimental design, and the PGW methodology. Section. 3 presents the simulated changes in the TC characteristics and analyzes the mechanisms underlying these changes from both thermodynamic and dynamic perspectives. The discussion and conclusions are provided in Sections 4 and 5, separately.

2. Materials and methods

2.1. Overview of Typhoon case

Super Typhoon Usagi (2013) had a significant impact on the China south coastal regions. To illustrate its characteristics, Figs. 1 and 2 show the track and intensity of the Super Typhoon Usagi (2013) across the Western Pacific Ocean. The track and intensity data is based on best-track data from the China Meteorological Administration (CMA) (Lu et al., 2021; Ying et al., 2014). Usagi formed as a tropical depression southwest of Okinotori-Shima Island at 06 UTC on 16 September 2013 and moved slowly eastward. After turning westward over the same waters, it strengthened to tropical storm intensity at 18 UTC on 16 September. Usagi continued moving westward and was upgraded to typhoon intensity east of the Philippines at 12 UTC on 18 September. The formation process occurred under an extremely warm ocean with water temperatures exceeding 30 °C and weak vertical wind shear of 4 m s^{-1} (Liu et al., 2018). Usagi underwent rapid intensification, achieving severe typhoon status by 06 UTC on 19 September and reaching Super typhoon intensity 6 h later. During the rapid intensification, the wind speeds increased by 33 m s^{-1} within a 24-h period (Zhao et al., 2016; Liu et al., 2018). It peaked with maximum wind speeds (MWS) of 60 m s^{-1} and a minimum sea level pressure (MSLP) of 915 hPa around 06 UTC on 20 September 2013. Continuing a west-northwestward track, Usagi passed through the Luzon Strait and

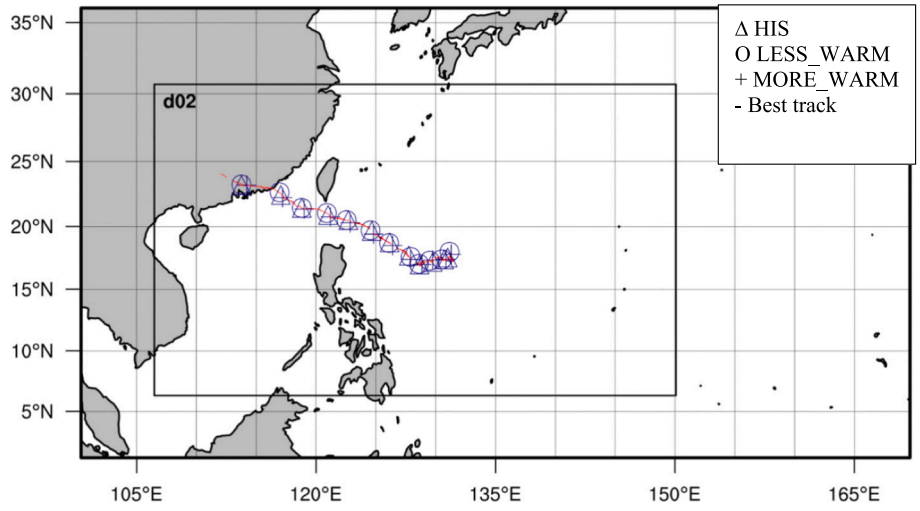

Fig. 1. Domains used in this study, with the outer domain having a 25 km horizontal resolution and the inner domain having with a 5 km resolution. The red dashed lines represent the best track of Super Typhoon Usagi (2013) from CMA. Symbols indicate the simulated TC locations: "+" for MORE_WARM, "○" for LESS_WARM, and "△" for the HIS. The HIS simulation reproduces Usagi's northwestward track and landfall with biases generally <50 km compared to best track data from CMA, while LESS_WARM and MORE_WARM scenarios show minimal changes from HIS. (For interpretation of the references to colour in this figure legend, the reader is referred to the web version of this article.)

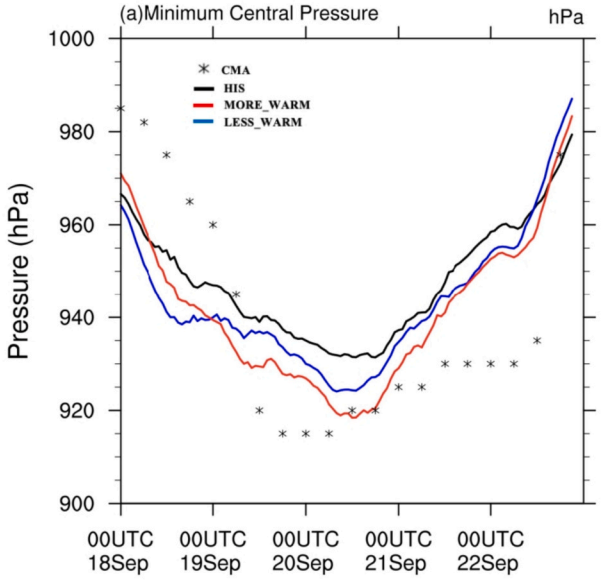

Fig. 2. Comparison of the time series of the minimum central pressure (hPa) simulated for Super Typhoon Usagi from 00 UTC on 1800 September 2013 to 2100 UTC on 22 September 2013 for historical simulation (HIS, black), MORE_WARM (red), LESS_WARM (blue), CMA best track (*). Future projections (MORE_WARM and LESS_WARM) show a strengthening trend with lower peak pressures (5–10 hPa). Differences between MORE_WARM and HIS are statistically significant at the 1 % level, and differences between LESS_WARM and HIS are significant at the 5 % level, based on a Student's *t*-test. (For interpretation of the references to colour in this figure legend, the reader is referred to the web version of this article.)

entered the South China Sea on 21 September. It made landfall in the southern part of China with typhoon intensity the next day. It maintained strong winds of approximately 45 m s^{-1} at landfall, and was accompanied by extreme rainfall, with 224 meteorological stations recording daily precipitation totals between 100 and 250 mm (CMA, 2013). Although its peak intensity was relatively lower than that of Super Typhoon Mangkhut (2018)—a Category 5 typhoon widely studied due to its extreme wind and surge impacts—Usagi made landfall during an astronomical high tide, leading to exceptionally high observed tidal levels (e.g., 3.38 m at Tsim Bei Tsui vs. 4.18 m during Mangkhut; HKO, 2013). Finally Usagi weakened to tropical depression intensity by 00 UTC on 23 September, and dissipated at 0600 UTC the next day.

2.2. Model description, settings and validity

The Advanced Research Weather Research and Forecasting (WRF-ARW) model , version 4.3.3 (Skamarock et al., 2019), is widely used for dynamical downscaling studies. This high-resolution model can represent convection and the other physical processes that are essential for a TC system (Moon et al., 2018), making it well-suited for present study. Based on previous sensitivity research on horizontal resolution (Gentry and Lackmann, 2010; Sun et al., 2013; Gutmann et al., 2018; Delfino et al., 2023), the model was configured with two domains: 25 km and 5 km. The domain setup is adopted here due to balance computational cost and are suitable for resolving different scales of TC structure. The domains are illustrated in Fig. 1, with a regional grid of 295 × 160 grid points for the outer domain and 925 × 550 for the inner domain, covering the entire TC track. This first domain encompasses most regions of the Northwest Pacific region, while the second domain covers the southern coastal regions of China and part of southeast Asia, areas frequently impacted by TCs. The model top was set at 50 hPa, with 52 sigma layers in the vertical direction. For shortwave and longwave radiation, the Dudhia (Dudhia, 1989) and the Rapid Radiative Transfer Model (RRTM) (Mlawer et al., 1997) schemes were used respectively. For the planetary boundary layer scheme, we used the Yonsei University (YSU) nonlocal PBL scheme (Hong et al., 2006) with a surface boundary layer scheme based on Zhang and Anthes (1982). For land surface processes, the unified Noah Land Surface Model (Chen and Dudhia, 2001) was used. Regarding the cumulus and microphysics processes, which significantly impact on TC simulation, models with 5 km horizontal resolution in the "grey zone" cannot fully resolve the detailed structure of deep convection in tropical regions (Lin et al., 2024; Yin et al., 2022). Therefore, for this study, we used the Kain-Fritsch (KF) cumulus scheme (Kain, 2004) for the inner domain and WRF Single-Moment 6-class (WSM6) microphysics scheme (Hong et al., 2004). Previous studies (e.g., Delfino et al., 2023; Sun et al., 2024) have shown that WRF simulation with varying the initialization time can introduce differences in simulated TC intensity. Such differences arise from model internal variability, as small perturbations in the initial conditions can grow nonlinearly during the model integration, even under identical large-scale forcing. However, these differences are generally small compared with the magnitude of the projected climate change signal (Lee et al., 2023; Delfino et al., 2023). In addition, Sun et al. (2024) indicate that simulations initialized at an earlier stage when the TC Usagi was weaker (e.g., tropical depression and tropical storm stage) exhibited smaller differences (within 1 hPa) in simulated TC intensity attributable to model internal variability, as well as reduced bias relative to observations. Thus, in this study, the initialization time was determined based on the CMA best-track dataset, which indicates that the TC first reached tropical storm intensity (maximum sustained wind speed >17 m s^{-1}) at that time. This choice is consistent with previous studies that initiated simulations when the TC attained comparable intensity (Sun et al., 2013; Delfino et al., 2022). The simulation was initiated at 18 UTC on 16 September 2013, and the total duration was 150 h, running until 00 UTC on 23 September 2013. The first 12 h are treated as the model spin-up period. This study focuses on the period from 2013 to 09-18 00 UTC to 2013-09-22 12 UTC, during which the tropical cyclone reached and maintained typhoon intensity, including the periods of severe precipitation.

Spectral nudging is widely used in historical TC downscaling and climate projection studies to maintain TC tracks close to observations, facilitating attribution analyses (e.g., Delfino et al., 2022; Gutmann et al., 2018; Chen et al., 2020; Tran et al., 2022). Delfino et al. (2022) showed that nudging reduced TC track bias by ~20 km with minimal impact on intensity, but excessive nudging can suppress TC intensification (Cha et al., 2011). Nudging configurations vary across studies in terms of variables, vertical level, and spectral cutoff. For example, Chen et al. (2020) nudged above 500 hPa with a 1000 km cutoff to constrain large-scale steering while avoiding interference with inner-core circulations. Moon et al. (2018) recommended nudging humidity only above 800 hPa due to limited influence on TC dynamics. Applying nudging at scales larger than ~1000 km preserves mesoscale and convective variability while constraining synoptic features (Gómez and Miguez-Macho, 2017). Based on these studies, we used a conservative approach: nudging only horizontal winds above 500 hPa with a 1000 km cutoff and a coefficient of 0.0003 s^{-1}, minimizing interference with the TC's internal evolution.

For the historical run (HIS), the initial and boundary conditions were derived from 0.25° spatial resolution and 6-h temporal resolution reanalysis data from the fifth-generation global reanalysis of the European Centre for Medium-Range Weather Forecasts (ERA5; Hersbach et al., 2020). Land surface information was obtained from the 20 land use classifications Moderate Resolution Imaging Spectroradiometer (MODIS) satellite dataset.

Regarding the validity of the model, the simulated historical track and intensity of Super Typhoon Usagi (2013) were compared with the CMA best-track data. To evaluate the performance of simulated rainfall, we used the Integrated Multi-satellitE Retrievals for GPM (IMERG) Final Run product (Version 07) with a half-hourly time resolution and 0.1° x

0.1°spatial resolution (Huffman et al., 2023). This data is commonly used for the validation of TC rainfall simulations (Lee et al., 2023; Pamintuan and Bagtasa, 2025).

2.3. PGW method and selected Forcing Data

To assess how Super Typhoon characteristics respond to global warming, we use the PGW method to simulate the TC case under future climate scenarios. This PGW method uses initial and boundary conditions derived from the ERA5 dataset, with perturbations added based on fields from various GCMs. To explore the sensitivity of TC projections to model warming responses, we select two GCMs representing the high- and low-sensitivity extremes of the CMIP6 ensemble rather than using MMEs. Climate sensitivity is characterized by the equilibrium climate sensitivity (ECS; Meehl et al., 2020), defined as the long-term equilibrium global mean temperature change following a doubling of pre-industrial carbon dioxide concentrations. The high-sensitivity model, CanESM5 (ECS ≈ 5.6; Swart et al., 2019), shows a large tropospheric warming of 2.5–10 K (Fig. S1a). The low-sensitivity model, INM-CM5–0 (ECS ≈ 1.9; Volodin et al., 2017), shows a much smaller warming of 0.5–3 K (Fig. S1a). Both models exhibit minimal relative humidity change in the boundary layer (Fig. S1b). This high–low model pairing captures the sensitivity of PGW-simulated TC responses to the choice of GCMs under SSP5–8.5 forcing.

The variables perturbed in the forcing data include SST, Ta, RH, horizontal winds (U, V), pressure and geopotential height. In this study, climate perturbations were derived from CMIP6 simulations under the high-emission scenario SSP5–8.5, based on monthly climatologies for the far-future period (2070–2099) and the historical baseline (1985–2014). The PGW deltas were computed by subtracting the historical monthly means from the future monthly means for each variable, thereby capturing seasonally varying climate change signals. Horizontally, the resulting PGW deltas were interpolated to match the spatial resolution of the ERA5 reanalysis and added to the ERA5 fields used for both initial and lateral boundary conditions. Vertically, the perturbations were computed on the native pressure levels of the CMIP6 models and then directly mapped to the corresponding pressure levels in the ERA5 fields without vertical interpolation. This approach preserves the high-frequency diurnal and synoptic variability provided by ERA5, while embedding the low-frequency climate change signal derived from the monthly GCM anomalies. The overall workflow of this PGW downscaling procedure is illustrated in Fig. S2.

2.4. Tracking algorithm

The tracking algorithm used in this study is adopted from Gutmann et al. (2018). However, in this study, the 400 km × 400 km evaluation box around the storm center is substituted by a 2° x 2° (inner-core) and a 5° x 5° box on a regular lon-lat grid. As Patricola and Wehner (2018) mentioned that precipitation increases near the TC center and drying in the outer TC radii, which can lead to different results depending on the box size. Liu et al. (2019) also found varying results using different box sizes. The TC center is detected by the algorithm is the minimum central pressure in the region.

2.5. Diagnostics to assess the impact of global warming

To quantify the response of TC to global warming, we first examined changes in TC track, intensity. Intensity is assessed through minimum central pressure. Next, we analyzed the response of total precipitation and hourly precipitation rates. Furthermore, we investigated key thermodynamic and dynamic variables that respond to climate change signals. Thermodynamic variables include spatial changes of SST, air-sea fluxes (latent and sensible heat flux), vertical profiles of Ta, water vapor, hydrometeors, equivalent potential temperature (convective stability). Dynamic variables include vertical profiles of wind field structures (tangential wind, radial wind, and vertical velocity), and vertical wind shear (environmental factor). Building on these qualitative assessments of thermodynamic and dynamic structures, we next performed a quantitative analysis of TC precipitation. We assessed changes in TC precipitation scaling rate relative to the CC relation, which predicts that saturated specific humidity increases by roughly 7 % per °C rise in temperature. To quantify the sensitivity of TC rainfall to warming, we computed the precipitation scaling rate with respect to SST, following previous studies (e.g., Liu et al., 2019; Knutson et al., 2020; Tran et al., 2024), given its strong coupling with near-surface air temperature in tropical ocean environments. Changes in SST and latent heat flux were calculated as the differences in the mean values within a 5° × 5° box centered on the TC. Changes in precipitable water (PW), updrafts, and downdrafts were calculated as the differences in the mean values within a 2° × 2° box centered on the TC, consistent with the spatial scale used for precipitation rate analysis. Updrafts and downdrafts were defined using the positive and negative vertical velocities at 500 hPa, respectively. In addition, the moisture flux convergence (MFC; unit in kg/(m^2·s·hPa)) is calculated as the negative of the divergence of the vapor transport:

$$MFC_{850} = -\left(\frac{\partial(q_{850}u_{850})}{\partial x}+\frac{\partial(q_{850}v_{850})}{\partial y}\right) \quad (1)$$

q850: specific humidity (kg kg^{-1}) at the 850 hPa level, representing the mass of water vapor per unit mass of air. u850, v850 (m s^{-1}): horizontal wind components at 850 hPa, representing zonal (east-west) and meridional (north-south) wind speeds, respectively.

Furthermore, the changes in moisture flux convergence can be decomposed into two main terms: advection and convergence term. Here we further decomposed the convergence term into three terms based on Seager et al. (2010) and Ngai et al. (2024):

$$-\Delta\langle q\cdot D\rangle = -\langle q_{\text{hist}}\cdot\Delta D\rangle - \langle \Delta q\cdot D_{\text{hist}}\rangle - \langle \Delta q\cdot \Delta D\rangle \quad (2)$$

q is the specific humidity, D represents divergence. ⟨⟩ Is the vertical integration from surface pressure to the top-of-atmosphere pressure. Δ denotes the future change relative to the historical period (future minus historical). The subscript 'hist' means the historical simulation. The three terms on the right-hand side of Eq. (2) represent the dynamic contribution associated with changes in atmospheric circulation, thermodynamic contribution related to the changes in specific humidity (moisture content), and the non-linear term influenced by the changes in both circulation and moisture content.

3. Results

3.1. Track and Intensity changes

In the HIS simulation, the model accurately simulated Usagi's northwestward track across the Philippine Sea and subsequent landfall in southern China, exhibiting track bias approximately within 50 km relative to CMA best-track data (Fig. 1). Future projections under both LESS_WARM and MORE_WARM scenarios indicate minimal changes in TC track characteristics relative to HIS simulations.

As for historical intensity simulation, the model captures the evolution of the Super Typhoon Usagi (2013), capturing both its intensification phase (characterized by decreasing minimum central pressure) and subsequent decay phase (marked by rising pressure, Fig. 2). The model output shows the intensification from 966 hPa at 00 UTC 18 Sep to peak intensity (approximately 930 hPa) by 12 UTC 20th Sep (intensification period), and follows by decaying. The results shows a generally reasonable agreement with the CMA best-track data, despite a slight overestimation (underestimation) in TC minimum central pressure (intensity). Regarding bias of TC intensity in HIS simulation, our results indicate a systematic underestimation in peak intensity. Such biases are commonly reported in previous studies involving WRF-based TC

simulations. For example, Previous WRF simulations of super typhoons show varying intensity biases, ranging from 3.4 to 10.8 hPa for Hato (Ma et al., 2023), 24.7–27.5 hPa for Mangkhut (Pamintuan and Bagtasa, 2025), and up to 44 hPa for Haiyan (Delfino et al., 2022). Similarly, Lee et al. (2023) and Sun et al. (2019) reported general underestimations of TC intensity in WRF simulations, attributing them to limitations in the ERA5 and NCEP FNL reanalysis datasets, respectively, in representing storm structures at initialization. The model resolution also have large impacts on the simulated TC intensity. As resolution is increased, minimum central pressure decreases significantly (by 30 hPa from 8 to 1 km grid spacing, Gentry and Lackmann (2010)). In addition, the simulations were not able to capture Usagi's rapid intensification phase as other strong TC like Haiyan (2013) in previous studies (Delfino et al., 2022). However, as pointed out by Chen et al. (2020), the discrepancies between historical simulations and observations do not directly undermine the assessment of TC responses to climate change, since these are based on the relative differences between historical and future scenarios rather than absolute intensity values. Therefore, although a certain degree of underestimation exists in the historical simulation of TC intensity, the bias falls within a range comparable to those reported in earlier studies and is considered acceptable for the purpose of investigating future projections.

In future projections, both LESS_WARM and MORE_WARM exhibit consistent decrease in the minimum central pressure by approximately 5–10 hPa at the peak intensity compared to HIS run (Fig. 2). This decrease of pressure indicates further promotes rapid intensification and sustains stronger TCs under future climate conditions. To further test the robustness of our findings, we conducted three additional PGW experiments using different CMIP6 GCMs (AWI-CM-1-1-MR, KIOST-ESM, and MPI-ESM1–2-LR) under the SSP5–8.5 scenario. All the experiments consistently showed an increase in typhoon intensity, demonstrating the robustness of the TC intensification (not shown here).

3.2. Precipitation changes

The spatial distribution of accumulated precipitation from the HIS simulation shows general agreement with IMERG observations (Fig. 3a-b), particularly in capturing the overall orientation and location of the primary rainbands. However, noticeable differences remain near the eyewall, where the HIS simulation overestimates both the magnitude and compactness of the extreme rainfall core compared to IMERG. Previous studies also found that the WRF model tends to simulate heavier precipitation than IMERG (Lee et al., 2023). It should also be noted that satellite-based precipitation products themselves have considerable uncertainty (Lee et al., 2023). Given this observational uncertainty, the WRF model can still be considered to exhibit reasonable skill in simulating TC precipitation. To further minimize the influence of model biases on climate change attribution, the present study focuses on the relative differences between the warming and control experiments (e.g., MORE_WARM vs. HIS), rather than absolute precipitation values.

We examined the spatial pattern of accumulated precipitation of Super Typhoon Usagi in HIS and the difference with two WARM experiments (Fig. 3). The distribution of the precipitation band closely correlates with the TC tracks, which exhibit minimal shifts across the three experiments as depicted in Fig. 1. Consequently, the spatial location of precipitation remains relatively similar across these experiments. Compared with minimal shifts in track, there has been a significant alteration in the amount of accumulated precipitation. Compared with HIS, both LESS_WARM and MORE_WARM show an increase in precipitation along the TC track. MORE_WARM exhibits an expansion of precipitation region exceeding 500 mm in HIS run. Additionally, in certain regions historically experiencing precipitation between 300 mm and

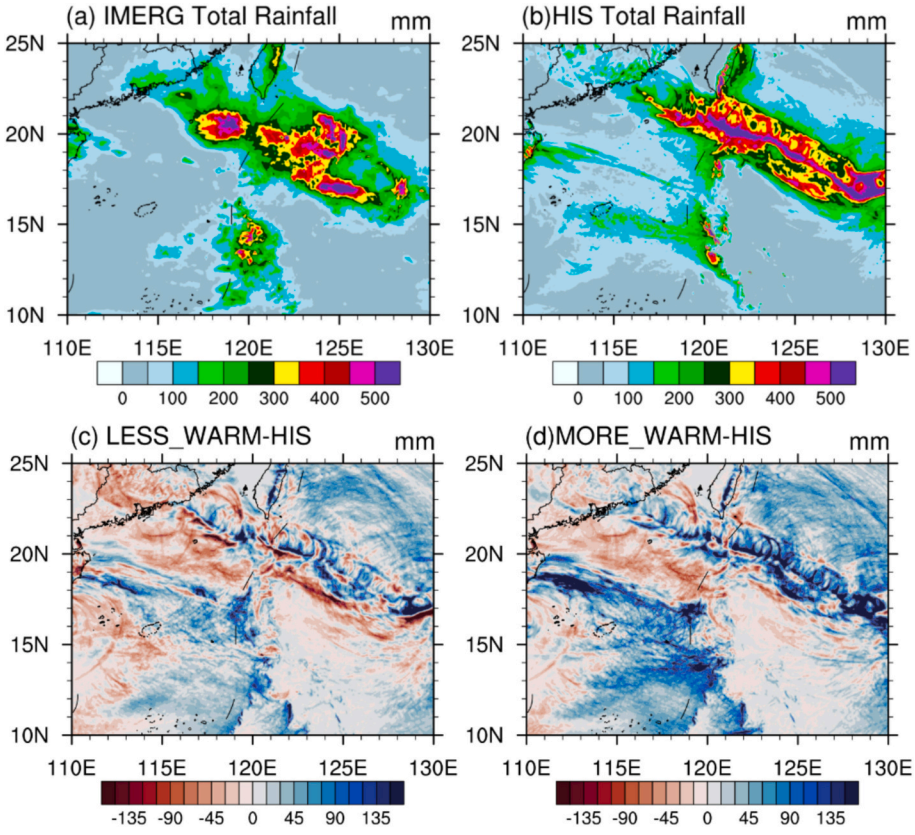

Fig. 3. Spatial patterns of accumulated precipitation (mm) for Usagi from 00 UTC on 18 September 2013 to 23 UTC on 23 September 2013 as observed by (a) IMERG and and simulated by (b) HIS, (c) LESS_WARM, and (d) MORE_WARM experiments. The HIS (b) generally reproduces the observed precipitation band (a). Compared to HIS, both LESS_WARM (c) and MORE_WARM (d) show increased precipitation along the track.

450 mm, the precipitation has increased to over 450 mm in MORE_WARM. Precipitation changes in coastal landing areas remain relatively unchanged. LESS_WARM also demonstrates an increase in precipitation, albeit less intensely compared to MORE_WARM. The increase in extreme precipitation area is qualitatively consistent with previous study results for extreme precipitation events (Lee et al., 2023).

To specifically show the temporal changes in precipitation intensity, we examined the regional average hourly precipitation within a box along the TC center, as shown in Fig. 4. From 00 UTC on the 18th to 12 UTC on the 20th Sep, the precipitation intensity shows an increasing trend (Figs. 4a), align with TC intensification (TC intensity increases as the Minimum Central Pressure decreases, as shown in Fig. 2). After the first peak, the two subsequent peak values are relatively weak compared to the first one. The precipitation peaks may be related to the typhoon' s intensification and evolution into a triple-eyewall structure (Zhao et al., 2016). However, the model cannot accurately reproduce this intensification process, although it might capture the general intensification.

The peak precipitation rate for MORE_WARM and LESS_WARM is 29 mm h^{-1} and 26 mm h^{-1}, respectively, compared to the HIS of 21 mm h^{-1} (Fig. 4a). The average hourly precipitation rate in MORE_WARM and LESS_WARM increases by 26.4 % and 6.5 % compared to HIS (Fig. 4b). Notably, MORE_WARM demonstrates a 40 % increase during the hour of peak precipitation intensity, whereas LESS_WARM exhibits a 25 % increase (Fig. 4b). Employing the 6°box (not shown), we also found an increase in precipitation, although the increase is relatively weaker compared to 2° box results. These results are consistent with that previous study by Patricola and Wehner (2018) that precipitation increases near the TC center and drying in the outer TC radii when comparing with varying box size. Fig. 3 also confirms that the outer TC radii shows some decrease in precipitation.

3.3. Potential Vorticity changes

TC is a positive potential vorticity (PV) anomaly in the atmospheric flow environment (Lackmann, 2015). The enhanced cyclonic PV maximum is consistent with increased TC intensity, as demonstrated by the spatial PV patterns in Fig. 5a–c. Compared with HIS, both LESS_WARM and MORE_WARM shows spatially increases in PV. Fig. 5d employs the probability density distribution (PDF) to quantify the increase in PV, showing that compared to the HIS scenario, the MORE_WARM and LESS_WARM scenarios exhibit increases in the maximum value of the PDF from 15 to approximately 26 and 20, respectively.

3.4. Sea surface temperature, moisture, and air-sea heat flux changes

To further analyze the mechanism behind the enhancement of TC intensity, precipitation and potential vorticity, we examined moist thermodynamic state changes in the ocean and sea surface. SST changes is projected to be between 0.6 and 3.6 K warmer compared to the HIS in simulation period under the SSP5–8.5 scenario (Fig. 6a–b). Fig. 6c–d shows that MORE_WARM and LESS_WARM produced around 4.0 g kg^{-1} and 1.5 g kg^{-1} water vapor mixing ratio increase respectively, which is close to previous studies (Gutmann et al., 2018, 4 g kg^{-1}; Delfino et al., 2023, 1.5 g kg^{-1}). This warmer and wetter surface could supply more energy from ocean to air, which could drive the intensification of TC (Gutmann et al., 2018; Delfino et al., 2023).

To quantify the energy exchange between air and ocean, we further examined air-sea heat flux changes. Latent heat flux is a main heat source for TC development (Sun et al., 2019). Latent heat flux (Fig. 6e–f) has a larger increase in the experimental domain. MORE_WARM and LESS_WARM produce more latent heat flux (approximately 60–90 W m^{-2} and 30–60 W m^{-2} respectively) under a warming climate.The sensible heat flux does not change much under a warming climate compared to HIS (Fig. 6g–h). These results consistent with previous study that the TC intensification is driven by more latent heat flux supplied from a warmer ocean in the future (Delfino et al., 2023; Chen et al., 2020; Nakamura et al., 2016)).

3.5. Air temperature and water vapor: Vertical profile and time changes

We further examined the box-average time changes in the vertical profiles of air temperature and water vapor due to warming climate. There is a significant decrease in low-level RH in WARM scenarios around TC center (Fig. 7a–c). This is expected because only a drier low-level atmosphere (especially BL) will lead to more latent heat flux (Fig. 6e–f), thus lead to stronger TCs. The vertical profile of air temperature changes (Fig. 7d–f) shows the increase in upper troposphere air temperature, which will to some extent offset the TC intensification, despite the more latent heat flux from the surface. More latent heat flux from ocean will lead to the increase in water vapor content in

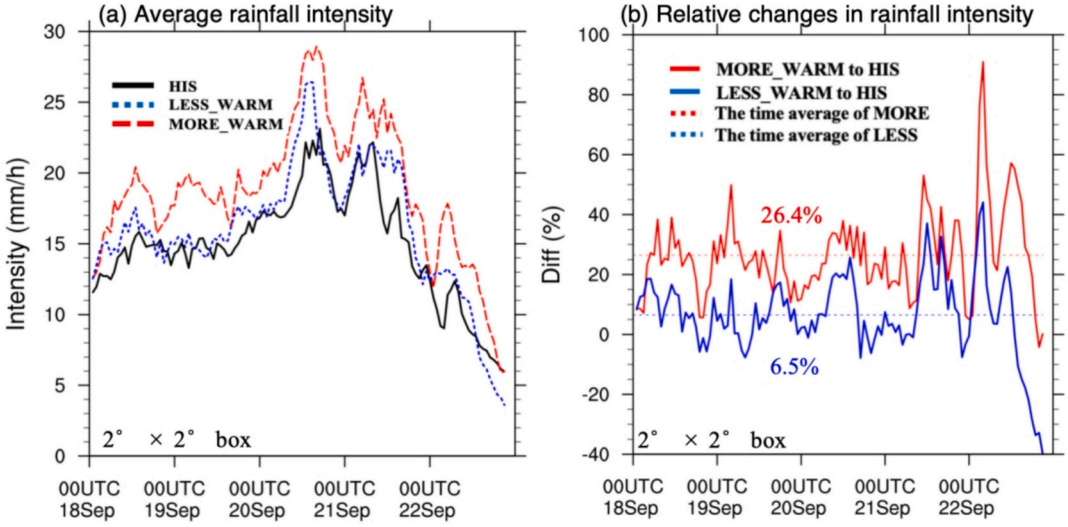

Fig. 4. Comparison of simulated (a) regional average hourly precipitation rate (mm h^{-1}) time series and (b) relative changes from a 2° box for Usagi from 00 UTC on 1800 September 2013 to 2100 UTC on 22 September 2013 for HIS (black), MORE_WARM (red), LESS_WARM (blue). Compared to HIS (black), MORE_WARM (red) and LESS_WARM (blue) show higher peak rates of 29 mm h^{-1} and 26 mm h^{-1}, respectively, representing increases of 26.4 % and 6.5 % in average hourly precipitation. Differences between MORE_WARM and HIS are statistically significant at the 1 % level, and differences between LESS_WARM and HIS are significant at the 5 % level, based on the Student's *t*-test. (For interpretation of the references to colour in this figure legend, the reader is referred to the web version of this article.)

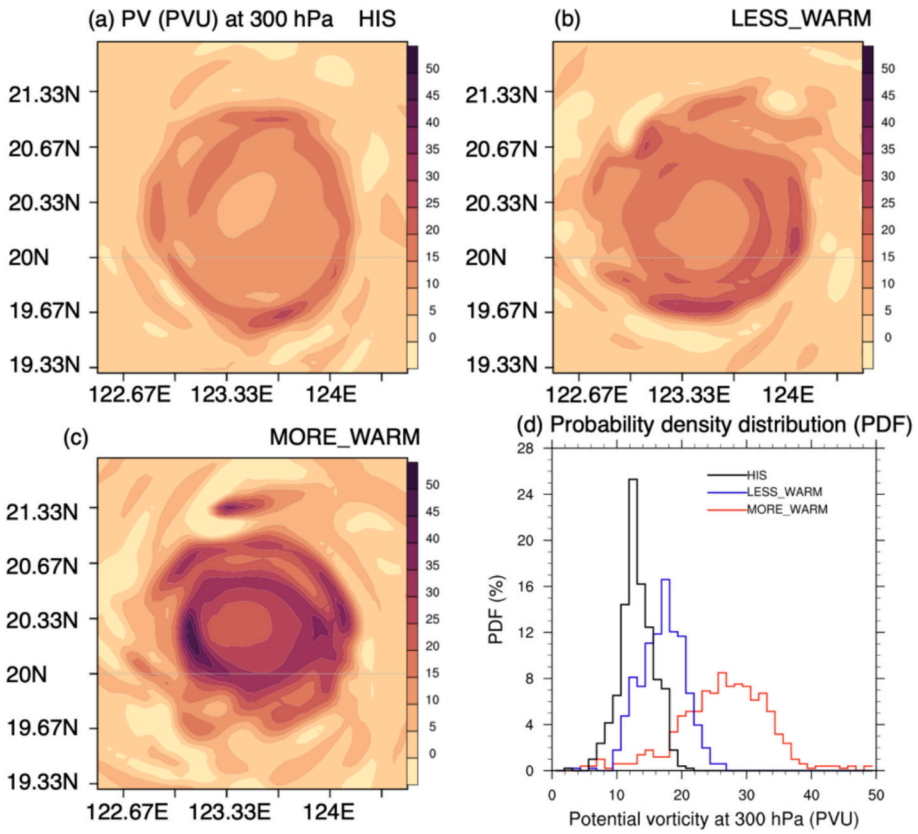

Fig. 5. Spatial distribution potential vorticity (PV) differences at 300 hPa between MORE_WARM (c), LESS_WARM (b), and HIS (a) on Sep 20th at 12 UTC for Typhoon Usagi and probability density distribution of PV (d). The TC appears as a positive PV anomaly, with enhanced cyclonic PV maxima corresponding to stronger TC intensity under warming climate.

atmosphere, which is beneficial for extreme precipitation. MORE_WARM in comparison increased by 4.8–6 g kg^{-1} (24–30 %) and LESS_WARM by 1.2–3.6 g kg^{-1} (6–18 %) compared to HIS (20 g kg^{-1}) (Fig. 7g–i). Notably, the large increase of water vapor at a low-level happens during the intensification period.

Moreover, different hydrometers exhibit contrasting responses near the freezing levels, within the cloud, and near the cloud top due to warming climate. In this study, liquid condensate (cloud, and rain) mixing ratios increase below the freezing level by 0.1–0.5 g kg^{-1} (Fig. 8a–f). Previous studies have suggested that raindrops fall faster than snow or ice, thereby enhancing downdrafts and intensifying precipitation due to a higher concentration of liquid condensate (Yuter et al., 2006; R. Rasmussen et al., 2011). Meanwhile, a comparison of the mixing ratio of solid condensate (snow and ice) reduce by 0.1–0.4 g kg^{-1} between 6 and 10 km altitude in the WARM scenarios compared to the HIS but increase at a similar level between 10 and 16 km (Fig. 8g-l). This implies that freezing occurs at a higher altitude due to warming and rising cloud tops, which benefits for stronger rainfall (Lin et al., 2024). Additionally, the mixing ratio of graupel increases above 6 km height but decreases below it, which could be a result of the rising freezing level (Fig. 8m-o). These changes in atmospheric hydrometers associated with global warming favor increase in precipitation.

3.6. Wind structure changes

Warming also significantly alters the dynamic structure of TCs. Fig. 9 shows the azimuth average radius-height cross-sections of tangential winds, radial wind, and vertical velocity for the three simulations respectively. The azimuth average maximum tangential wind speed increases from 50 to 60 m s^{-1} to up to more than 65 m s^{-1} with an outward and upward expansion of the region of stronger wind speed (Fig. 9a–c). The azimuth average radial wind also tends to be stronger both in convergence (inflow) near the surface and divergence (outflow) at the upper layer (Fig. 9d–f). The increased low-level radial inflow enhances moisture convergence for storm precipitation production (Liu et al., 2019). The increase of the vertical velocity from 6 to 8 Pa s^{-1} to up to more than 10 Pa s^{-1} which means a stronger eyewall updraft (Fig. 9g–i). Besides, the outside convection in future scenarios is also stronger than the HIS. This increase in vertical velocity in the upper troposphere is associated with the increase of tropopause height-induced TC eyewalls to become taller (Yamada et al., 2017). Above all, the increase in tangential wind suggests a stronger primary circulation, and the increase of inflow and outflow as well as broader eyewall updraft suggests a stronger secondary circulation.

3.7. Thermodynamic and dynamic contribution

To quantify the mechanisms contributing to the increased precipitation in our simulations, we analyzed key thermodynamic and dynamic variables within the TC center (Table 1). Compared to the HIS, both the LESS_WARM and MORE_WARM simulations show notable increases in precipitation, with mean rates of 16.0 mm hr^{-1} (6.5 %) and 18.8 mm hr^{-1} (26.4 %), respectively. This enhancement is accompanied by higher SST (0.6–2.9 K) and increased LH (10.1–14.3 %), indicating a stronger thermodynamic environment. The values in first row of brackets in Table 1 represent the estimated increase in moisture based on the SST-induced CC scaling (4.2 %–20.3 %). While the increases in PW and precipitation in the LESS_WARM and MORE_WARM simulations (8.5 %–33.3 %, 6.5 %–26.4 % respectively) exceed these theoretical estimates, indicating that thermodynamic effects alone cannot fully account for the simulated intensification. Dynamic contributions are also evident, as updraft and downdraft speeds increase by 12–31 % relative to HIS, while

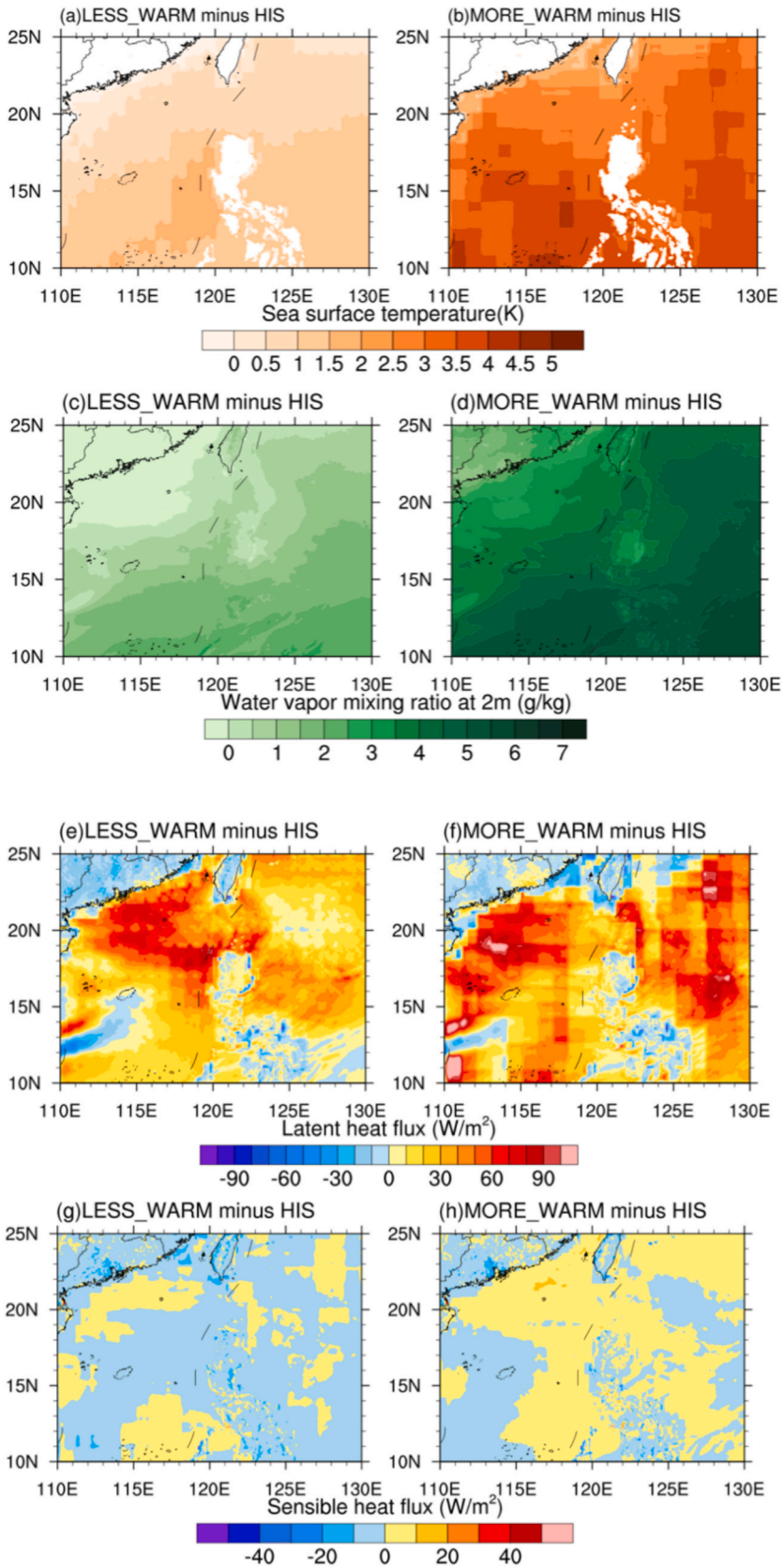

Fig. 6. Spatial SST variations, heat flux, and water vapor mixing ratio changes compared Between MORE_WARM, LESS_WARM, and HIS: (a–b) SST changes (K);(c–d) 2-m water vapor mixing ratio (g kg-1); (e-f) average latent heat flux (W m^{-2}); (g-h) average sensible heat flux (W m^{-2}) for Usagi from 0000 UTC on 18 September 2013 to 2300 UTC on 23 September 2013. Compared to HIS, MORE_WARM and LESS_WARM show warmer SST (0.6–3.6 K), higher water vapor (1.5–4.0 g kg^{-1}), and increased latent heat flux (30–90 W m^{-2}), supporting stronger TC intensification, while sensible heat flux remains largely unchanged.

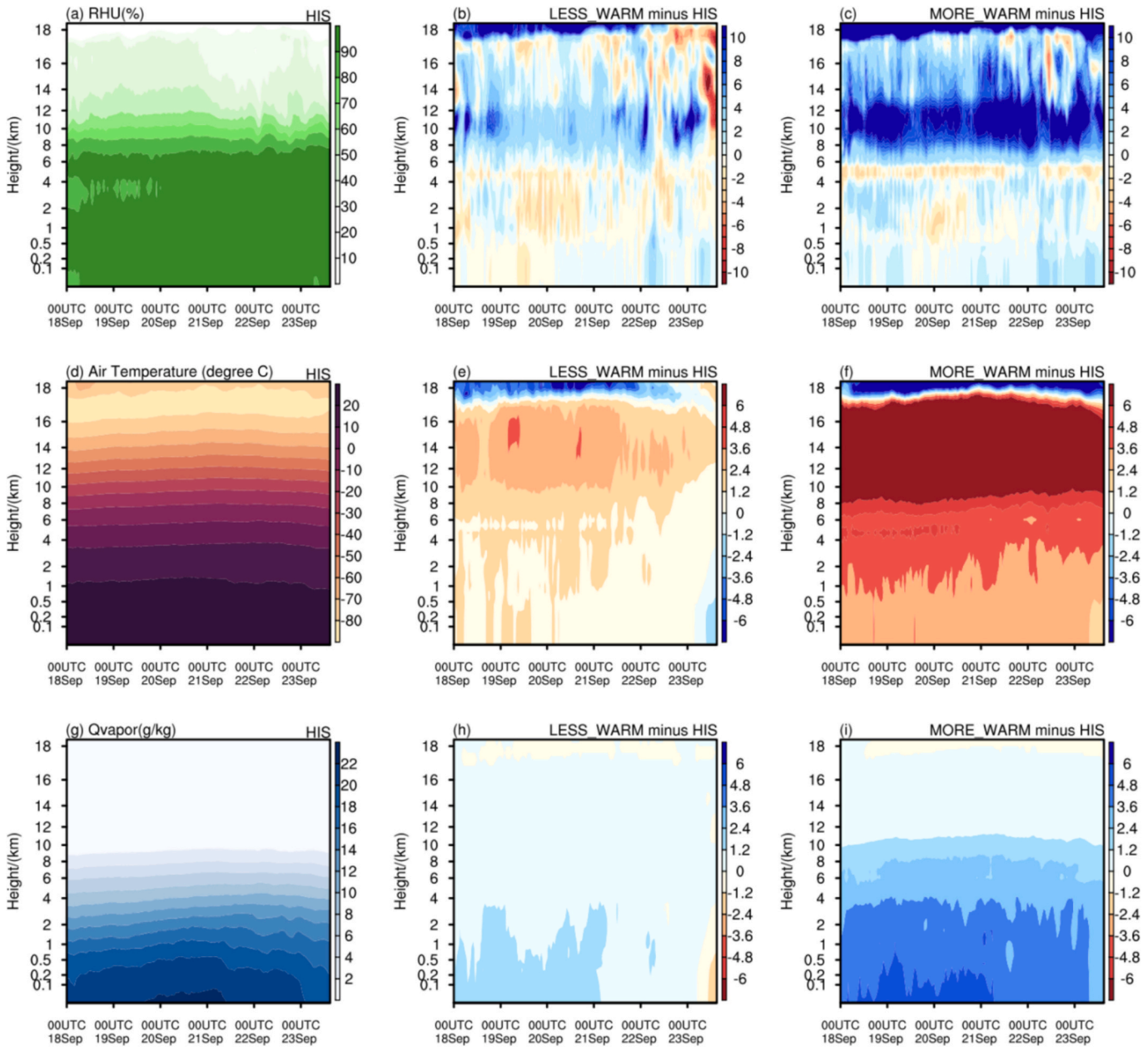

Fig. 7. The changes of vertical profiles in time series around 2° box average in (a–c) relative humidity (%), (d–f), air temperature (°C),(g–i) water vapor mixing ratio (g kg-1) from HIS (left), and the difference between LESS_WARM (middle), MORE_WARM (right) respectively. Compared to HIS, WARM scenarios show decreased low-level RH, increased upper-troposphere temperature, and enhanced low-level water vapor (1.2–3.6 g kg^{-1} in LESS_WARM, 4.8–6 g kg^{-1} in MORE_WARM), promoting stronger TC intensification and extreme precipitation.

MFC shows a corresponding rise. These results suggest that both thermodynamic and dynamic factors synergistically contribute to the intensification of precipitation.

In addition, we quantified the relative contributions of dynamic, thermodynamic, and nonlinear processes to the observed changes in moisture convergence, as shown in Fig. 10. For the LESS_WARM scenario, the contributions from dynamic, thermodynamic, and nonlinear terms were 21.5 %, 61.1 %, and 17.4 %, respectively, indicating that thermodynamic processes dominated the precipitation increase, while dynamics also played a substantial role. For the MORE_WARM scenario, the corresponding contributions were 8.7 %, 86.4 %, and 4.9 %, suggesting an even stronger thermodynamic control under warmer conditions. The nonlinear term, although smaller, captures interactions between dynamic and thermodynamic effects. Overall, these results highlight that both thermodynamic and dynamic processes synergistically influence the moisture convergence changes in the TC center, ultimately modulating precipitation intensity.

4. Discussion

4.1. Estimation of TC intensity changes

Most PGW downscaling studies consistently suggest that TCs in the WNP are projected to intensify, as reflected by decreases in minimum sea level pressure (SLP) (Tran et al., 2022; Chen et al., 2020, 2022; Delfino et al., 2023). Our analysis shows that the minimum SLP of Super Typhoon Usagi decreases by approximately 5–10 hPa under the PGW scenario. Chen et al. (2020) applied PGW simulations using CMIP5 output and reported minimum SLP reductions of 16.9 hPa for TC Hagupit, 10 hPa for TC Victor, and 5 hPa for TC Utor by the late 21st

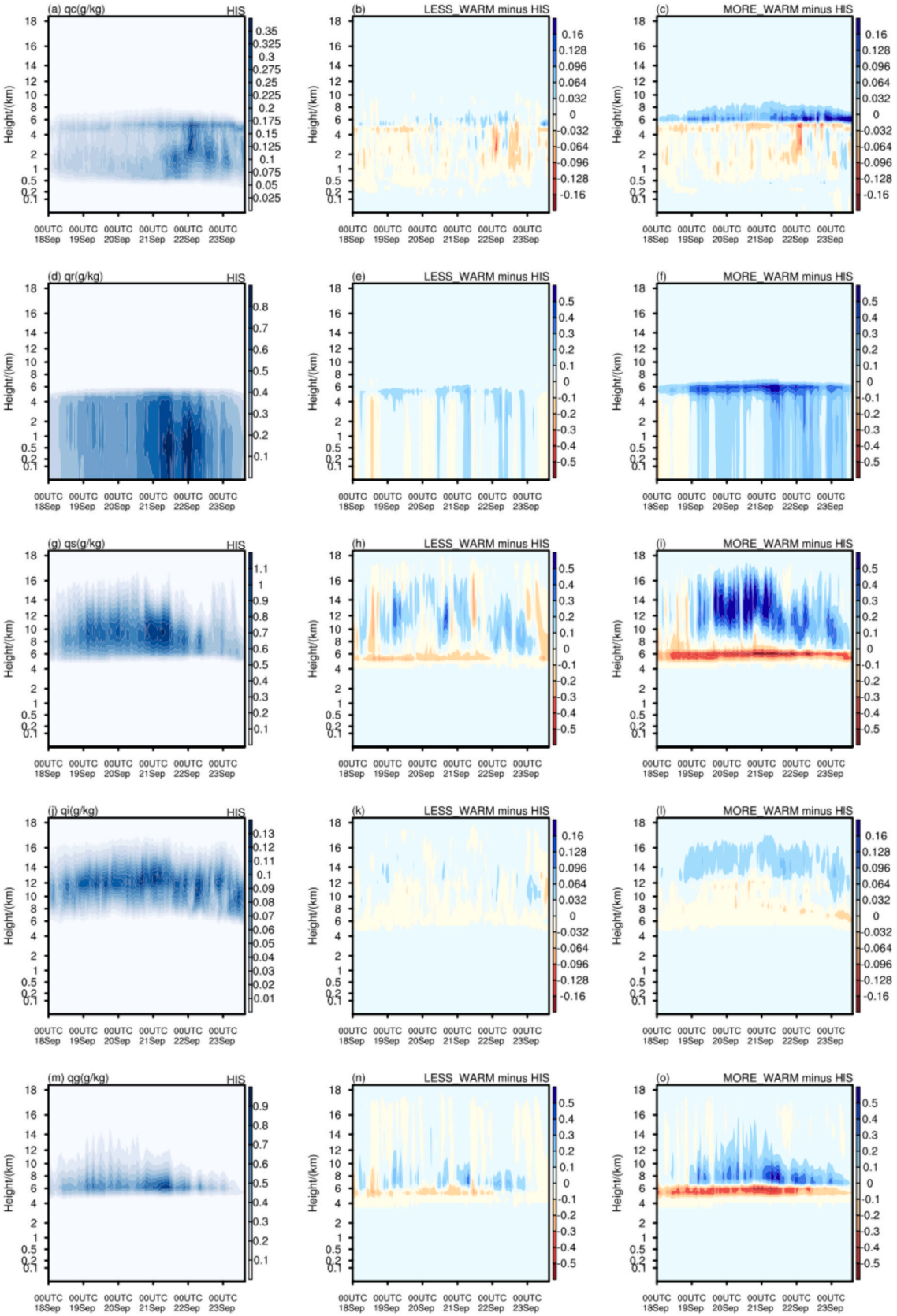

Fig. 8. The changes of vertical profiles in time series around 2° box average in the simulated mixing ratio of cloud (a–c), rain water (d–f), snow (g–i), ice (j–l), graupel (m–o) (g kg-1) from HIS (left), and the difference between LESS_WARM (middle), MORE_WARM (right) respectively. In WARM scenarios, liquid condensate (cloud and rain) increases below the freezing level (0.1–0.5 g kg^{-1}), solid condensate (snow and ice) decreases between 6 and 10 km but increases above 10 km, and graupel increases above 6 km, indicating higher freezing levels and cloud tops, which favor stronger precipitation.

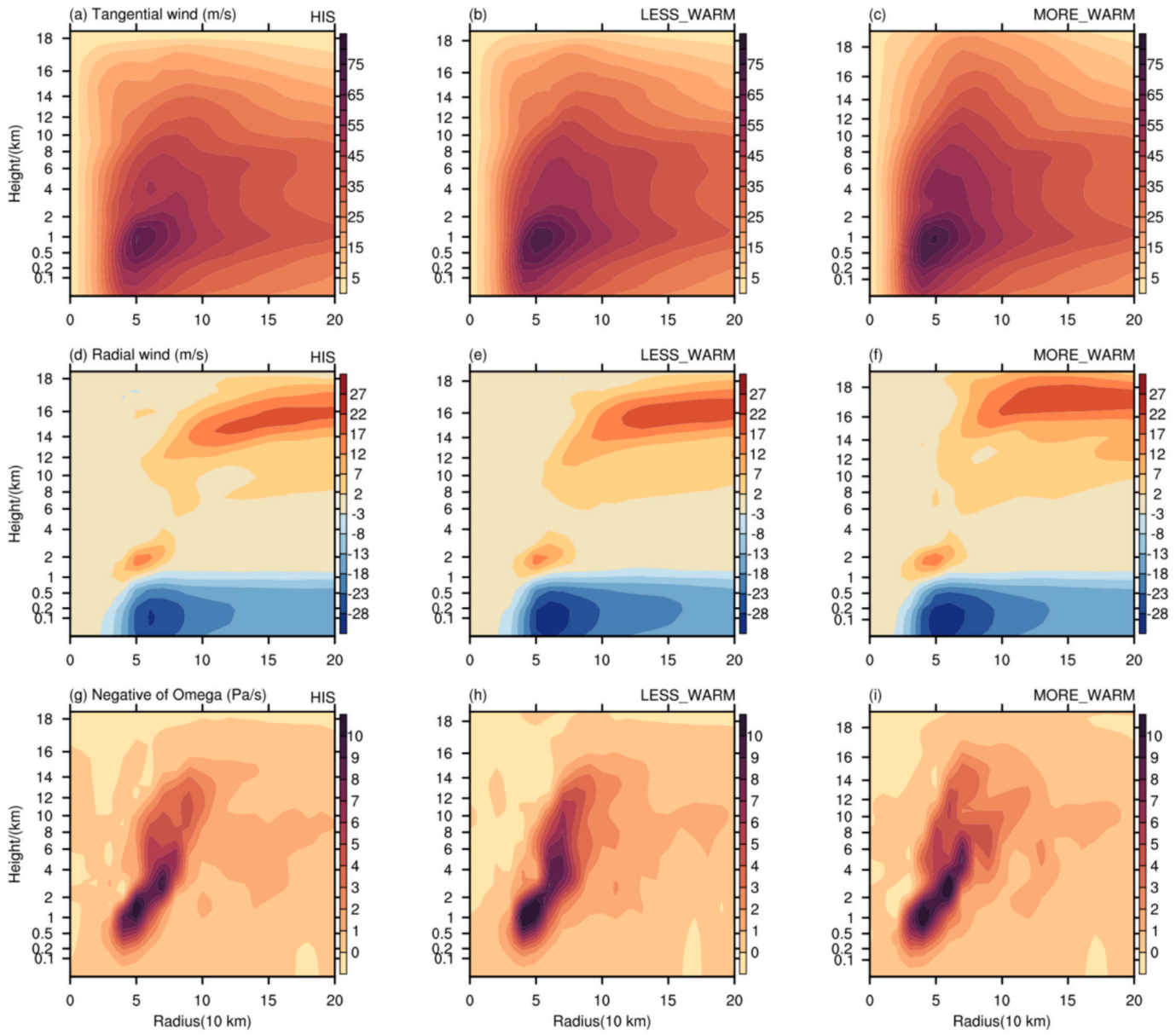

Fig. 9. Azimuth average radius–height cross sections for TC Usagi on Sep 20th at 00 UTC. Thin black lines are (a–c) tangential velocity (m s^{-1}), (d–f) radial velocity (m s^{-1}), and (g–i) vertical velocity (Pa s^{-1}). Panels a, d, and g show the results of HIS, panels b, e, h, and panels c, f, i show those of LESS_WARM and MORE_WARM, respectively. Compared to HIS, WARM scenarios show stronger tangential winds (50–65 m s^{-1}), enhanced low-level inflow and upper-level outflow, and increased eyewall updrafts (6–10 Pa s^{-1}), indicating intensification of both primary and secondary circulation and taller eyewalls.

century (2075–2099). Using CMIP6-based PGW experiments, Tran et al. (2022) found an average decrease of ~9.25 hPa (0.99 %) in minimum SLP by the 2090s. Delfino et al. (2023), employing a 5 km WRF configuration, projected decreases of 4 hPa, 1 hPa, and 11 hPa in minimum SLP for TCs Haiyan (2013), Bopha (2012), and Mangkhut (2018), respectively, under SSP5–8.5. The magnitude of projected minimum SLP decreases varies among studies and individual cases. Our results show slightly smaller decreases compared with previous PGW studies, which may partly reflect the influence of model resolution. For example, Delfino et al. (2023) compared simulations at 5 km and 3 km grid spacing and found that the higher-resolution (3 km) runs captured more pronounced decreases in minimum SLP, indicating that finer resolution tends to simulate stronger TC intensification. The relatively weaker intensification in our case may partly reflect seasonal timing, as the climate change signal incorporated in PGW experiments can vary substantially by month. In particular, the increase in stability is slightly greater in September and October than in July and August (Gutmann et al., 2018), which may influence the magnitude of TC intensification. These factors highlight the sensitivity of projected TC intensity changes to modeling resolution choices, storm characteristics, and timing, underscoring the importance of case-specific analyses for landfalling TCs in the southern coastal regions of China.

4.2. *Estimation of precipitation changes*

Most PGW downscaling studies consistently suggest that TCs in the WNP are projected to produce more precipitation (Tran et al., 2022; Chen et al., 2022). In our simulations, precipitation rates increase by ~6.5 %–26.4 %, slightly exceeding the CC scaling (4.2 %–20.3 %). Chen et al. (2022) similarly reported inceased TC rainfall, with extreme precipitation within the eyewall (95th percentile and above) strengthening by 22 % ± 12 %. Tran et al. (2024) found precipitation increases of 15 %–35 % from the outer to the inner core, with a ~ 25.7 % increase within 100 km of the center, also exceeding the CC rate (14.1 % for 2.1 K

Table 1
Changes in box-average values of thermodynamic, dynamic parameters between current and future Climates including Precipitation (Precip), SST, Latent heat flux (LH), Precipitable water (PW), Updraft and Downdraft at 500 hPa, and moisture convergence flux (MFC). Statistical significance assessed using Student's *t*-test: $p < 0.10$ (*), $p < 0.05$ (**), $p < 0.01$ (***).

Variables	HIS	LESS_WARM		MORE_WARM	
	mean	mean	Diff(%)	mean	Diff(%)
Precip (mm h)	15.0	16.0	6.5** (4.2 %)	18.8	26.4*** (20.3 %)
SST (K)	296.0	296.6	0.6 K	298.9	2.9 K*
LH (W/m^2)	265.5	292.3	10.1***	303.5	14.3***
PW (kg/m^2)	75.7	82.1	8.5***	100.9	33.3***
Updraft (m s^{-1})	0.58	0.65	12.1***	0.72	24.1***
Downdraft (m s^{-1})	0.19	0.22	15.8***	0.25	31.6***
MFC (10^{-5} kg/(m^2·s·hPa)	4.98	5.26	5.6*	6.46	29.7***

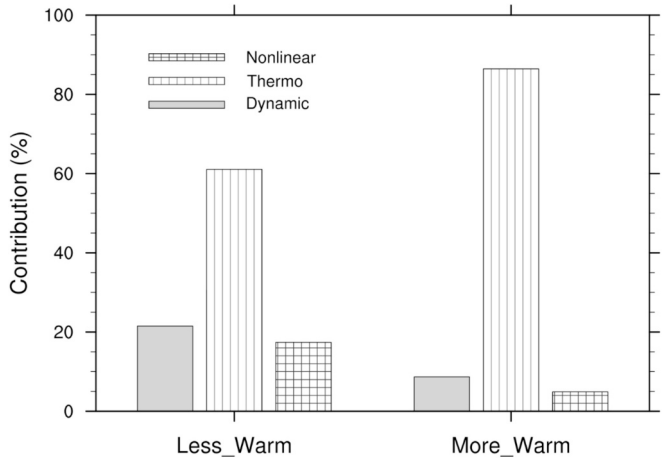

Fig. 10. Relative Contributions of Dynamic, Thermodynamic, and Nonlinear Terms to Changes in Moisture Convergence within the TC center; thermodynamic effects dominate (61–86 %), dynamics contribute moderately (9–22 %), and nonlinear interactions are minor (5–17 %).

warming). In contrast, Gutmann et al. (2018) reported ~24 % increases in maximum rainfall rates within 400 km × 400 km region, consistent with the increase in water vapor predicted by the CC relation (22 % for 3.2 K) over the Gulf of Mexico. Despite the general agreement on increased TC-induced rainfall, discrepancies arise when examining the radial structure of precipitation and the magnitude of rainfall rate increases. Differences across studies may arise from the precipitation metric and the radial definition relative to the storm center. For example, Tran et al. (2024) highlighted that precipitation changes vary radially, peaking near the storm center, and results depend on whether rainfall is calculated using fixed radii, circle-averages, or radial-averages. Additional differences may stem from storm characteristics, such as track, translation speed, and TC size. In our case, changes in track and translation speed are negligible, but the storm size becomes slightly more compact (Fig. 5), likely leading to modest inward shifts of the radius of maximum rainfall. This response is consistent with the findings of Tran et al. (2024), who also reported inward shifts of peak rainfall under warming conditions.

Additionally, averaging across a large number of cases without considering the varying intensities and durations of individual TC events could also induce the discrepancy. Liu et al. (2019) and Tran et al. (2024) both found that strong TC exhibit the most significant increased rainfall across future states compared to weaker TC. Future research is needed to verify whether our results hold for cyclones of varying strengths and occurring in different seasons (pre- vs. post-monsoon) in the WNP region.

4.3. Mechanims analysis

In the WNP region, Chen et al. (2020) and Delfino et al. (2023) have reported that the increase in SST, latent heat flux, moist mid-troposphere, thus higher convective available potential energy (CAPE) with decrease in vertical wind shear, which is quite important for the increase in TC intensity. Similarly, we observed an increase in SST, latent heat flux and moist air (Fig. 6e-f and Table 1) along the TC track. In addition, equivament potential temperature and higher convective instability height (Fig. S3). However, when examining the impact of VWS from the synoptic environment (Fig. S4), we found small changes, the results may differ from previous research (Delfino et al., 2023) that demonstrated changes in VWS, suggesting potential variability across different cases.

The intensification of TCs and the precipitation increase exceeding the CC rate under warming are closely tied to coupled thermodynamic and dynamic processes. Warmer SSTs elevate atmospheric moisture content in line with CC scaling, but the simulated precipitation increase in the TC core surpasses this thermodynamic expectation, indicating additional dynamic contributions (Table 1 and Fig. 10). Enhanced low-level inflow and radial convergence transport larger amounts of warm, moist air toward the eyewall, while stronger updrafts driven by latent heating accelerate vertical moisture transport (Table 1 and Fig. S5). These processes synergistically amplify convection and secondary circulation, promoting compact eyewall and intensification of tangential winds (Fig. 9), which in turn feed back positively to further increase rainfall rates beyond CC scaling. These mechanisms are consistent with the findings of Tran et al. (2024).

4.4. Limitations and future directions

However, comparing the magnitude of these changes remains challenging due to variability arising from differences in GCM selection (large variations in SST and air temperature), climate scenarios (RCP or SSP), TC case studies (intensity, genesis, seasonality, and track), and model configurations (domain resolution, cumulus, and microphysics parameterization combination, initial time), including the use of the PGW method (perturbation variables).

We acknowledge the limitation that using only two GCMs is insufficient to fully quantify the impacts of climate change on TC characteristics. Ideally, a larger ensemble of GCMs would help to better represent the full range of structural uncertainty. Due to computational and data storage constraints, we were not able to conduct PGW experiments using a large ensemble of GCMs. Instead, we adopted an ECS-based selection strategy, in line with Delfino et al. (2023) and Jones et al. (2023), to capture a range of warming responses using two representative GCMs—one with relatively low ECS (LESS_WARM) and one with high ECS (MORE_WARM). As SST changes are among the dominant factors affecting TC intensity in PGW studies (e.g., Patricola and Wehner, 2018; Delfino et al., 2023; Lavender et al., 2018), this selection aims to provide a preliminary understanding of the sensitivity of TC intensity and precipitation to different warming levels. To enhance the robustness of our findings, we conducted three additional PGW experiments using CMIP6 GCMs: AWI-CM-1-1-MR, KIOST-ESM, and MPI-ESM1–2-LR. Across these additional simulations, the projected changes in TC intensity consistently show an increase, supporting the robustness of our earlier results and further demonstrating the sensitivity of TC responses to different GCM forcings. This sensitivity-based approach highlights the GCMs selection in modulating TC intensity and precipitation projections, and demonstrates the utility of incorporating diverse GCMs to assess the structural uncertainties inherent in PGW frameworks.

As for domain selection, a horizontal resolution of ~5 km is

commonly used in WRF TC simulations. For example, Lackmann (2015) conducted sensitivity experiments of Hurricane Ivan (2004) with grid spacings between 12 and 2 km and found partial convergence of TC structure and intensity at 8–4 km, with intensity differences of only ~10 hPa. Similarly, Sun et al. (2013) simulated Typhoon Shanshan (2006) at grey-zone resolutions (7.5–1 km) and reported relatively small intensity changes between 5 and 3 km, but a marked increase when the resolution was further refined to 1 km. Delfino et al. (2022) and Gutmann et al. (2018) also adopted inner domains of 5 km and 4.5 km, respectively. In general, convection must be parameterized at resolutions coarser than ~10–5 km, whereas convection-permitting resolutions (~4–5 km) allow explicit representation. Additional simulations at 4.5 km resolution showed no significant difference in TC intensity compared with coarser setups (Delfino et al., 2022). Based on these findings, we employed a 5 km horizontal resolution in this study, striking a balance between computational efficiency and realistic representation of TC structure.

Notably, at 5 km, deep convection begins to be partially resolved by model dynamics, and retaining cumulus parameterization may introduce issues such as double counting of convective processes. Nonetheless, the application of cumulus schemes at kilometer-scale resolutions remains debated within the TC modeling community, as this scale lies within the so-called "grey zone," where both resolved and subgrid processes influence turbulence. In this study, we still use the KF scheme at 5 km resolution, supported by several considerations: (1) Previous studies (e.g., Delfino et al., 2022) have demonstrated that applying the KF scheme at 5 km resolution yields stronger TC intensities—approximately 15 hPa lower minimum sea level pressure—in Typhoon Haiyan (2013) over the Western North Pacific. This result aligns more closely with best-track intensity data compared to simulations using other cumulus parameterizations. Furthermore, comparisons with 4.5 km convection-permitting simulations showed no significant differences in TC representation. (2) Our preliminary analyses (Sun et al., 2024; Figs. 6b, 8d, and 10d) indicate that using the cumulus parameterization scheme at 5 km resolution does not substantially affect the simulated peak intensity, landfall wind, or precipitation of Super Typhoon Usagi (2013). (3) Recent studies (e.g., Wang et al., 2025) have investigated the impact of scale-aware cumulus schemes—including Grell–Freitas (GF), Grell-3 (G3), and simulations without any cumulus scheme—on kilometer-scale WRF simulations of typhoons such as Mujigae (2015), Hato (2017), and the Category 5 Mangkhut (2018). These studies found that cumulus scheme selection had limited influence on Mangkhut's precipitation, while relative errors varied for Mujigae and Hato depending on the scheme. For Mujigae, GF reduced relative error by 25 % compared to G3 at the 120 mm threshold, whereas for Hato, G3 performed better. This suggests that scale-aware cumulus schemes do not universally improve TC precipitation simulations. Additionally, simulations without cumulus schemes may produce spurious precipitation relative to those using the G3 scheme.

Despite the overall good performance of the simulations, underestimation of TC intensity remains a notable limitation. TC intensities were consistently underestimated, especially for Super Typhoons, due to the initial and boundary conditions provided by reanalysis datasets such as ERA5 and NCEP FNL (Lee et al., 2023; Sun et al., 2019), which may be attributed to their relatively coarse horizontal resolution (approximately 25 km for ERA5 and 100 km for FNL) and the sparse distribution of observations over the ocean. To mitigate the errors, simulations were started at an earlier stage when Usagi was still a tropical storm based on the CMA best-track dataset, which has been shown to reduce biases relative to observations (Delfino et al., 2023; Sun et al., 2024). Hodges et al. (2017) noted that improvements in TC representation in reanalysis datasets are largely associated with higher model resolution, enhanced data assimilation, and better-calibrated observing systems. In the future, further enhancements, including the integration of additional in situ and radar observations as well as AI-based downscaling methods (Zhang et al., 2024; Li et al., 2025), could improve the accuracy of initial and boundary fields for high-resolution TC simulations.

There are more constraints of our study.Firstly, we chose to focus on an in-depth analysis and comparison of a single storm event, using only two representative GCM perturbation inputs due to computational resource limitations. This approach was chosen to allow for a more detailed discussion of one example within a representative range of plausible future scenarios, as opposed to conducting long-term simulations. Secondly, we did not couple the ocean model to account for SST dynamic effects, such as cold tides. This limitation is also noted by Mittal et al. (2019) and Patricola and Wehner (2018) because of the the cold wake induced by TC winds can lead to a cooling of upper-ocean temperatures, providing a negative feedback on TC intensity. Additionally, due to our regional modeling nudging setting, this study cannot account for the remote influence of the large-scale atmospheric circulation patterns or the recurrent modes of climate variability affecting the western Pacific Ocean, which can impact the steering flow of the TCs. As a result, the TC track and translation speed show minimal change, which may not align with findings from global modeling research (Seneviratne et al., 2021). The simulated future TC frequency, track and translation speed response to climate change may not be realistic due to the limitation of the approach. This study rather focused on understanding the dynamic and thermodynamic influences of global warming on TC characteristics, including intensity and precipitation by controlling TC tracks as observed.

5. Conclusions

This study uses the high-resolution Weather Research and Forecasting (WRF) model with a 5 km horizontal resolution in the inner domain, driven by two representative GCMs from CMIP6 selected by ECS. The PGW method is employed to investigate how global warming impacts the intensity, precipitation, thermodynamic, and dynamic structure of strong landfalling Typhoon Usagi (2013) associated with compound-flood event. The main conclusions are as follows:

1. In a warming climate scenario compared to the historical run, the future simulations show an increase in intensity range from 5 hPa (Less_WARM) to 10 hPa (MORE_WARM).
2. The time-averaged increase in hourly precipitation rates ranges from 6.5 % (LESS_WARM) to 26.4 % (MORE_WARM), indicating substantial inter-GCM uncertainties that exceed the temperature-induced CC scaling (4.2 %–20.3 %).
3. From a thermodynamic perspective, the latent heat flux increases 30–90 W m^{-2} under different warmer (0.6–2.9 K SST) and wetter (1.5–4.0 g kg^{-1} water vapor mixing ratio) climate conditions, thereby providing more energy and enhancing the TC intensity. Warming may also alter the dynamic structure of TC, enhance vertical velocity (2–4 Pa s^{-1}), and tangential wind speed (5–10 m s^{-1}), and expand inflow and outflow regions.
4. The increase in precipitation exceeding the CC rate is driven by both thermodynamic and dynamic factors. In the MORE_WARM (LESS_WARM) scenario, the contributions from dynamic, thermodynamic, and nonlinear processes were 8.7 % (21.5 %), 86.4 % (61.1 %), and 4.9 % (17.4 %), respectively, indicating a dominant thermodynamic influence with a notable dynamic contribution.

Overall, these mechanisms are generally consistent across the GCMs used, but the magnitude of the changes varies. The high-ECS model shows stronger warming and moisture increase, leading to larger TC intensity changes, while the low-ECS model exhibits weaker responses. This highlights the uncertainty introduced by different GCMs, particularly due to their varying climate sensitivities, and underscores the importance of accounting for this variability when interpreting projected TC responses under climate change.

Future work will aim to incorporate multi-model ensembles and explore different downscaling methods (eg., Adachi and Tomita, 2020) to comprehensively address these uncertainties. Expanding the analysis

with more case studies and conducting long-term simulations of TC occurrences, coupled with ocean models, could further enhance understanding of ocean-atmosphere feedbacks. The findings such as increase TC intensity and precipitation rate, could also be utilized in hydrological and hydrodynamic models to improve future flood studies. Such intensification of TC winds and precipitation under climate warming poses heightened risks of compound flooding and greater challenges to disaster management.

Data and code availability

The fifth-generation global reanalysis of the European Centre for Medium-Range Weather Forecasts (ERA5) used for driving WRF experiments were downloaded from the ECMWF Climate DataStore (Hersbach et al., 2020). The monthly atmospheric temperature, relative humidity, geopotential height, and horizontal winds as well as skin temperature, sea surface temperature, and pressure data in the Coupled Model Intercomparison Project Phase6 (CMIP6) used for extracting the warming signal is available at WCRP-ESGF websites (Eyring et al., 2016). The best track data is from China Meteorological Administration (CMA)(https://tcdata.typhoon.org.cn/). The other data used in this study can be accessed by contacting the first author.

CRediT authorship contribution statement

Qi Sun: Writing – review & editing, Writing – original draft, Visualization, Validation, Software, Resources, Methodology, Investigation, Formal analysis, Data curation, Conceptualization. **Joël Arnault:** Writing – review & editing, Supervision, Investigation. **Christopher Holst:** Writing – review & editing, Supervision, Investigation. **Patrick Laux:** Writing – review & editing, Supervision, Investigation, Funding acquisition. **Harald Kunstmann:** Writing – review & editing, Supervision, Project administration.

Declaration of competing interest

The authors declare that they have no known competing financial interests or personal relationships that could have appeared to influence the work reported in this paper.

Acknowledgments

Qi Sun is supported financially by the China Scholarship Council (CSC). Joël Arnault is supported financially by German Research Foundation (DFG) through funding of the COSMIC Sense project. This work has been conducted in the framework of the MitRiskFlood project (01LP2005A) supported financially by the German Federal Ministry of Science of Education (BMBF). The simulations were conducted on the Linux cluster at KIT/ IMK-IFU in Garmisch-Partenkirchen. We would like to sincerely thank the editor and reviewers for their valuable comments and constructive suggestions, which have greatly improved the clarity and quality of our manuscript.

Appendix A. Supplementary data

Supplementary data to this article can be found online at https://doi.org/10.1016/j.atmosres.2025.108495.

Data availability

Data will be made available on request.

References

Adachi, S.A., Tomita, H., 2020. Methodology of the constraint condition in dynamical downscaling for regional climate evaluation: a review. J. Geophys. Res. Atmos. 125 (11), e2019JD032166. https://doi.org/10.1029/2019JD032166.

Barcikowska, M., Feser, F., Zhang, W., Mei, W., 2017. Changes in intense tropical cyclone activity for the western North Pacific during the last decades derived from a regional climate model simulation. Clim. Dyn. 49, 2931–2949. https://doi.org/10.1007/s00382-016-3420-0.

Bercos-Hickey, E., O'Brien, T.A., Wehner, M.F., Zhang, L., Patricola, C.M., Huang, H., Risser, M.D., 2022. Anthropogenic contributions to the 2021 Pacific Northwest heatwave. Geophys. Res. Lett. 49 (23), e2022GL099396. https://doi.org/10.1029/2022GL099396.

Brogli, R., Heim, C., Mensch, J., Sørland, S.L., Schär, C., 2023. The pseudo-global-warming (PGW) approach: methodology, software package PGW4ERA5 v1.1, validation, and sensitivity analyses. Geosci. Model Dev. 16, 907–926. https://doi.org/10.5194/gmd-16-907-2023.

Cha, D.-H., Jin, C.-S., Lee, D.-K., Kuo, Y.-H., 2011. Impact of intermittent spectral nudging on regional climate simulation using Weather Research and forecasting model. J. Geophys. Res. 116, D10103. https://doi.org/10.1029/2010JD015069.

Cha, E.J., Knutson, T.R., Lee, T.-C., Ying, M., Nakaegawa, T., 2020. Third assessment on impacts of climate change on tropical cyclones in the Typhoon Committee Region – Part II: Future projections. Tropical Cyclone Res. Rev. 9 (2), 75–86. https://doi.org/10.1016/j.tcrr.2020.04.005.

Chan, S.C., Kendon, E.J., Fowler, H.J., Kahraman, A., Crook, J., Ban, N., Prein, A.F., 2023. Large-scale dynamics moderate impact-relevant changes to organised convective storms. Commun. Earth Environ. 4, 8. https://doi.org/10.1038/s43247-022-00669-2.

Chen, F., Dudhia, J., 2001. Coupling an advanced land surface–hydrology model with the Penn State–NCAR MM5 modeling system. Part I: Model implementation and sensitivity. Mon. Weather Rev. 129, 569–585. https://doi.org/10.1175/1520-0493(2001)129<0569:CAALSH>2.0.CO;2.

Chen, J., Wang, Z., Tam, C.-Y., Lau, N.-C., Lau, D.-S.D., Mok, H.-Y., 2020. Impacts of climate change on tropical cyclones and induced storm surges in the Pearl River Delta region using pseudo-global-warming method. Sci. Rep. 10, 1965. https://doi.org/10.1038/s41598-020-58824-8.

Chen, J., Tam, C.Y., Wang, Z., Cheung, K., Li, Y., Lau, N.C., Lau, D.S.D., 2022. Future thermodynamic impacts of global warming on landfalling typhoons and their induced storm surges to the Pearl River Delta region as inferred from high-resolution regional models. J. Clim. 35 (15), 4905–4926. https://doi.org/10.1175/JCLI-D-21-0436.1.

Chih, C.H., Chou, K.H., Wu, C.C., 2022. Idealized simulations of tropical cyclones with thermodynamic conditions under reanalysis and CMIP5 scenarios. Geosci. Lett. 9, 33. https://doi.org/10.1186/s40562-022-00239-6.

Chih, C.H., Wu, C.C., Huang, Y.H., Li, Y.C., Shen, L.Z., Hsu, H.H., Liang, H.C., 2024. Intense tropical cyclones in the western North Pacific under global warming: a dynamical downscaling approach. J. Geophys. Res. Atmos. 129 (1), e2023JD038598. https://doi.org/10.1029/2023JD038598.

China Meteorological Administration (CMA), 2013. ESCAP/WMO Typhoon Committee 8th Integrated Workshop /2nd TRONG Forum Member Report. Available at: https://baike.baidu.com/wikiui/Main/referencepic?lemmaTitle=台风天兔&lemmaId=12000008&uuid=uNBGPBoF6JfM&versionId=652976725 (Accessed:June 27. 2025).

Delfino, R.J., Bagtasa, G., Hodges, K., Vidale, P.L., 2022. Sensitivity of simulating Typhoon Haiyan (2013) using WRF: the role of cumulus convection, surface flux parameterizations, spectral nudging, and initial and boundary conditions. Nat. Hazards Earth Syst. Sci. 22, 3285–3307. https://doi.org/10.5194/nhess-22-3285-2022.

Delfino, R.J., Vidale, P.L., Bagtasa, G., Hodges, K., 2023. Response of damaging Philippines tropical cyclones to a warming climate using the pseudo global warming approach. Clim. Dyn. https://doi.org/10.1007/s00382-023-06742-6.

Doan, Q., Chen, F., Kusaka, H., Dipankar, A., Khan, A., Hamdi, R., Roth, M., Niyogi, D., 2022. Increased risk of Extreme Precipitation over an Urban Agglomeration with Future Global Warming. Earths Future 10. https://doi.org/10.1029/2021EF002563.

Dougherty, E.M., Prein, A.F., Gutmann, E.D., Newman, A.J., 2023. Future simulated changes in Central U.S. mesoscale convective system rainfall caused by changes in convective and stratiform structure. J. Geophys. Res.-Atmos. 128. https://doi.org/10.1029/2022JD037537.

Dudhia, J., 1989. Numerical Study of Convection Observed during the Winter Monsoon Experiment using a Mesoscale Two-Dimensional Model. J. Atmos. Sci. 46, 3077–3107. https://doi.org/10.1175/1520-0469(1989)046<3077:NSOCOD>2.0.CO;2.

Emanuel, K., 2021. Response of global tropical cyclone activity to increasing CO2: results from downscaling CMIP6 models. J. Clim. 34, 57–70. https://doi.org/10.1175/JCLI-D-20-0367.1.

Eyring, V., Bony, S., Meehl, G.A., Senior, C.A., Stevens, B., Stouffer, R.J., Taylor, K.E., 2016. Overview of the coupled Model Intercomparison Project phase 6 (CMIP6) experimental design and organization. Geosci. Model Dev. 9, 1937–1958. https://doi.org/10.5194/gmd-9-1937-2016.

Gentry, M.S., Lackmann, G.M., 2010. Sensitivity of simulated Tropical Cyclone Structure and Intensity to Horizontal Resolution. Mon. Weather Rev. 138, 688–704. https://doi.org/10.1175/2009MWR2976.1.

Gómez, B., Miguez-Macho, G., 2017. The impact of wave number selection and spin-up time in spectral nudging: Wave Number selection and Spin-up Time in Spectral Nudging. Q. J. R. Meteorol. Soc. 143, 1772–1786. https://doi.org/10.1002/qj.3032.

Gutmann, E.D., Rasmussen, R.M., Liu, C., Ikeda, K., Bruyere, C.L., Done, J.M., Garrè, L., Friis-Hansen, P., Veldore, V., 2018. Changes in hurricanes from a 13-Yr convection-permitting pseudo–global warming simulation. J. Clim. 31, 3643–3657. https://doi.org/10.1175/JCLI-D-17-0391.1.

Guzman, O., Jiang, H., 2021. Global increase in tropical cyclone rain rate. Nat. Commun. 12 (1), 5344. https://doi.org/10.1038/s41467-021-25685-2.

Hersbach, H., Bell, B., Berrisford, P., Hirahara, S., Horányi, A., Muñoz-Sabater, J., Nicolas, J., Peubey, C., Radu, R., Schepers, D., Simmons, A., Soci, C., Abdalla, S., Abellan, X., Balsamo, G., Bechtold, P., Biavati, G., Bidlot, J., Bonavita, M., Chiara, G., Dahlgren, P., Dee, D., Diamantakis, M., Dragani, R., Flemming, J., Forbes, R., Fuentes, M., Geer, A., Haimberger, L., Healy, S., Hogan, R.J., Hólm, E., Janisková, M., Keeley, S., Laloyaux, P., Lopez, P., Lupu, C., Radnoti, G., Rosnay, P., Rozum, I., Vamborg, F., Villaume, S., Thépaut, J., 2020. The ERA5 global reanalysis. Q. J. R. Meteorol. Soc. 146, 1999–2049. https://doi.org/10.1002/qj.3803.

Hiraga, Y., Tahara, R., Meza, J., 2025. A methodology to estimate Probable Maximum Precipitation (PMP) under climate change using a numerical weather model. J. Hydrol. 652, 132659. https://doi.org/10.1016/j.jhydrol.2024.132659.

HKO, 2013. https://www.hko.gov.hk/tc/informtc/usagi/tabtide.htm.

Hodges, K., Cobb, A., Vidale, P.L., 2017. How well are tropical cyclones represented in reanalysis datasets? J. Clim. 30 (14), 5243–5264. https://doi.org/10.1175/JCLI-D-16-0557.1.

Hong, S.-Y., Dudhia, J., Chen, S.-H., 2004. A revised Approach to Ice Microphysical Processes for the Bulk Parameterization of Clouds and Precipitation. Mon. Weather Rev. 132, 103–120. https://doi.org/10.1175/1520-0493(2004)132<0103:ARATIM>2.0.CO;2.

Hong, S.-Y., Noh, Y., Dudhia, J., 2006. A new vertical diffusion package with an explicit treatment of entrainment processes. Mon. Weather Rev. 134, 2318–2341. https://doi.org/10.1175/MWR3199.1.

Huffman, G.J., Stocker, E.F., Bolvin, D.T., Nelkin, E.J., Tan, Jackson, 2023. GPM IMERG Final Precipitation L3 half Hourly 0.1 degree x 0.1 degree V07, Greenbelt, MD. In: Goddard Earth Sciences Data and Information Services Center (GES DISC). https://doi.org/10.5067/GPM/IMERG/3B-HH/07. Accessed: [30 th June, 2025].

Jiang, Y., Kim, J.B., Still, C.J., Kerns, B.K., Kline, J.D., Cunningham, P.G., 2018. Inter-comparison of multiple statistically downscaled climate datasets for the Pacific Northwest, USA. Sci Data 5, 180016. https://doi.org/10.1038/sdata.2018.16.

Jones, A.D., Rastogi, D., Vahmani, P., Stansfield, A.M., Reed, K.A., Thurber, T., Rice, J.S., 2023. Continental United States climate projections based on thermodynamic modification of historical weather. Sci Data 10 (1), 664. https://doi.org/10.1038/s41597-023-02485-5.

Kain, J.S., 2004. The Kain–Fritsch convective parameterization: An update. J. Appl. Meteorol. 43, 170–181. https://doi.org/10.1175/1520-0450(2004)043<0170:TKCPAU>2.0.CO;2.

Kimura, F., Kitoh, A., 2007. Downscaling by pseudo Global Warming Method (the Final Report of ICCAP). Research Institute for Humanity and Nature, Kyoto, Japan.

Knutson, T., Camargo, S.J., Chan, J.C., Emanuel, K., Ho, C.H., Kossin, J., Wu, L., 2020. Tropical cyclones and climate change assessment: Part II: projected response to anthropogenic warming. Bull. Am. Meteorol. Soc. 101 (3), E303–E322. https://doi.org/10.1175/BAMS-D-18-0194.1.

Knutson, T., Sirutis, J.J., Bender, M.A., Tuleya, R.E., Schenkel, B.A., 2022. Dynamical downscaling projections of late twenty-first-century US landfalling hurricane activity. Clim. Chang. 171 (3), 28. https://doi.org/10.1007/s10584-022-03346-7.

Knutson, T.R., Chung, M.V., Vecchi, G., Sun, J., Hsieh, T.L., Smith, A.J., 2021. Climate Change Is Probably Increasing the Intensity of Tropical Cyclones. Tyndall Centre for Climate Change Research.

Lackmann, G.M., 2015. Hurricane Sandy before 1900 and after 2100. Bull. Am. Meteorol. Soc. 96, 547–560. https://doi.org/10.1175/BAMS-D-14-00123.1.

Laux, P., Rötter, R.P., Webber, H., Dieng, D., Rahimi, J., Wei, J., Faye, B., Srivastava, A. K., Bliefernicht, J., Adeyeri, O., Arnault, J., 2021. To bias correct or not to bias correct? An agricultural impact modelers' perspective on regional climate model data. Agric. For. Meteorol. 304 (2021). https://doi.org/10.1016/j.agrformet.2021.108406. Article 108406.

Lavender, S.L., Hoeke, R.K., Abbs, D.J., 2018. The influence of sea surface temperature on the intensity and associated storm surge of tropical cyclone Yasi: a sensitivity study. Nat. Hazards Earth Syst. Sci. 18, 795–805. https://doi.org/10.5194/nhess-18-795-2018.

Lee, M., Min, S.-K., Cha, D.-H., 2023. Convection-permitting simulations reveal expanded rainfall extremes of tropical cyclones affecting South Korea due to anthropogenic warming. Npj Clim. Atmos. Sci. 6, 1–12. https://doi.org/10.1038/s41612-023-00509-w.

Li, S., Wan, H., Yu, Q., Wang, X., 2025. Downscaling of ERA5 reanalysis land surface temperature based on attention mechanism and Google Earth Engine. Sci. Rep. 15 (1), 675. https://doi.org/10.1038/s41598-024-83944-w.

Lin, Z., Nie, J., Wang, J., Chen, Y., Meng, Z., 2024. Responses of mesoscale convective system to Global Warming: a Study on the Henan 2021 Record-breaking rainfall event. J. Geophys. Res. Atmos. 129, e2023JD039473. https://doi.org/10.1029/2023JD039473.

Liu, M., Vecchi, G.A., Smith, J.A., Knutson, T.R., 2019. Causes of large projected increases in hurricane precipitation rates with global warming. Npj Clim. Atmos. Sci. 2, 38. https://doi.org/10.1038/s41612-019-0095-3.

Liu, S., Tao, D., Zhao, K., Minamide, M., Zhang, F., 2018. Dynamics and Predictability of the Rapid Intensification of Super Typhoon Usagi (2013). J. Geophys. Res.-Atmos. 123, 7462–7481. https://doi.org/10.1029/2018JD028561.

Lu, X., Yu, H., Ying, M., Zhao, B., Zhang, S., Lin, L., Bai, L., Wan, R., 2021. Western North Pacific Tropical Cyclone Database created by the China Meteorological Administration. Adv. Atmos. Sci. 38, 690–699. https://doi.org/10.1007/s00376-020-0211-7.

Lynn, B., Healy, R., Druyan, L., 2009. Investigation of Hurricane Katrina characteristics for future warmer climates. Clim. Res. - Clim. RES 39, 75–86. https://doi.org/10.3354/cr00801.

Ma, X., Li, J., Pang, S., Guo, T., Ding, C., 2023. Influence of surface layer schemes on tropical cyclone Hato (2017) intensity. J. Atmos. Sol. Terr. Phys. 250, 106110.

Manganello, J.V., Hodges, K.I., Dirmeyer, B., Kinter, J.L., Cash, B.A., Marx, L., Jung, T., Achuthavarier, D., Adams, J.M., Altshuler, E.L., Huang, B., Jin, E.K., Towers, P., Wedi, N., 2014. Future changes in the Western North Pacific tropical cyclone activity projected by a multidecadal simulation with a 16-km Global Atmospheric GCM. J. Clim. 27, 7622–7646. https://doi.org/10.1175/JCLI-D-13-00678.1.

Meehl, G.A., Senior, C.A., Eyring, V., Flato, G., Lamarque, J.-F., Stouffer, R.J., Taylor, K. E., Schlund, M., 2020. Context for interpreting equilibrium climate sensitivity and transient climate response from the CMIP6 Earth system models. Sci. Adv. 6, eaba1981. https://doi.org/10.1126/sciadv.aba1981.

Meiler, S., Ciullo, A., Kropf, C.M., Emanuel, K., Bresch, D.N., 2023. Uncertainties and sensitivities in the quantification of future tropical cyclone risk. Commun. Earth Environ. 4, 1–10. https://doi.org/10.1038/s43247-023-00998-w.

Mittal, R., Tewari, M., Radhakrishnan, C., Ray, P., Singh, T., Nickerson, A.K., 2019. Response of tropical cyclone Phailin (2013) in the Bay of Bengal to climate perturbations. Clim. Dyn. 53, 2013–2030. https://doi.org/10.1007/s00382-019-04761-w.

Mlawer, E.J., Taubman, S.J., Brown, P.D., Iacono, M.J., Clough, S.A., 1997. Radiative transfer for inhomogeneous atmospheres: RRTM, a validated correlated-k model for the longwave. J. Geophys. Res.-Atmos. 102, 16663–16682. https://doi.org/10.1029/97JD00237.

Moon, J., Cha, D., Lee, M., Kim, J., 2018. Impact of Spectral Nudging on Real-Time Tropical Cyclone Forecast. J. Geophys. Res.-Atmos. 123. https://doi.org/10.1029/2018JD028550.

Moon, Y., Kim, D., Wing, A.A., Camargo, S.J., Zhao, M., Leung, L.R., Moon, J., 2022. An evaluation of tropical cyclone rainfall structures in the HighResMIP simulations against satellite observations. J. Clim. 35 (22), 7315–7338. https://doi.org/10.1175/JCLI-D-21-0564.1.

Murakami, H., Vecchi, G.A., Underwood, S., Delworth, T.L., Wittenberg, A.T., Anderson, W.G., Zeng, F., 2015. Simulation and prediction of category 4 and 5 hurricanes in the high-resolution GFDL HiFLOR coupled climate model. J. Clim. 28 (23), 9058–9079. https://doi.org/10.1175/JCLI-D-15-0216.1.

Nakamura, R., Shibayama, T., Esteban, M., Iwamoto, T., 2016. Future typhoon and storm surges under different global warming scenarios: case study of typhoon Haiyan (2013). Nat. Hazards 82, 1645–1681. https://doi.org/10.1007/s11069-016-2259-3.

Ngai, S.T., Raghavan, S.V., Chung, J.X., Ona, B.J., Kimbrell, L.T., Nguyen, N.S., Liu, S., 2024. Relative contribution of dynamic and thermodynamic components on Southeast Asia future precipitation changes from different multi-GCM ensemble members. Adv. Clim. Chang. Res. 15 (5), 869–882. https://doi.org/10.1016/j.accre.2024.08.007.

Pamintuan, J.P.P., Bagtasa, G., 2025. Sensitivity of WRF tropical cyclone simulations in the Philippines to different SST data. Dyn. Atmos. Oceans 105, 101578. https://doi.org/10.1016/j.dynatmoce.2025.101578.

Park, D.S.R., Kim, H.S., Kwon, M., Byun, Y.H., Kim, M.K., Chung, I.U., Min, S.K., 2021. A performance evaluation of potential intensity over the tropical cyclone passage to South Korea simulated by CMIP5 and CMIP6 models. Atmosphere 12 (9), 1214. https://doi.org/10.3390/atmos12091214.

Parker, C.L., Bruyère, C.L., Mooney, P.A., Lynch, A.H., 2018. The response of land-falling tropical cyclone characteristics to projected climate change in Northeast Australia. Clim. Dyn. 51, 3467–3485. https://doi.org/10.1007/s00382-018-4091-9.

Pathak, R., Dasari, H.P., Ashok, K., Hoteit, I., 2023. Effects of multi-observations uncertainty and models similarity on climate change projections. Npj Clim. Atmos. Sci. 6, 1–12. https://doi.org/10.1038/s41612-023-00473-5.

Patricola, C.M., Wehner, M.F., 2018. Anthropogenic influences on major tropical cyclone events. Nature 563, 339–346. https://doi.org/10.1038/s41586-018-0673-2.

Pérez-Alarcón, A., Vázquez, M., Trigo, R.M., Nieto, R., Gimeno, L., 2024. Evaluation of WRF model configurations for dynamic downscaling of tropical cyclones activity over the North Atlantic basin for Lagrangian moisture tracking analysis in future climate. Atmos. Res. 307, 107498. https://doi.org/10.1016/j.atmosres.2024.107498.

Pierce, D.W., Cayan, D.R., 2016. Downscaling humidity with Localized Constructed Analogs (LOCA) over the conterminous United States. Clim. Dyn. 47, 411–431. https://doi.org/10.1007/s00382-015-2845-1.

Rasmussen, R., Liu, C., Ikeda, K., Gochis, D., Yates, D., Chen, F., et al., 2011. High-resolution coupled climate runoff simulations of seasonal snowfall over Colorado: a process study of current and warmer climate. J. Clim. 24 (12), 3015–3048. https://doi.org/10.1175/2010JCLI3985.1.

Rendfrey, T.S., Bukovsky, M.S., McCrary, R.R., Fuentes-Franco, R., 2021. An assessment of tropical cyclones in north American CORDEX WRF simulations. Weather Clim. Extr. 34, 100382. https://doi.org/10.1016/j.wace.2021.100382.

Roberts, M.J., Vidale, P.L., Senior, C., Hewitt, H.T., Bates, C., Berthou, S., Wehner, M.F., 2018. The benefits of global high resolution for climate simulation: process understanding and the enabling of stakeholder decisions at the regional scale. Bull. Am. Meteorol. Soc. 99 (11), 2341–2359. https://doi.org/10.1175/BAMS-D-15-00320.1.

Sato, T., Kimura, F., Kitoh, A., 2007. Projection of global warming onto regional precipitation over Mongolia using a regional climate model. J. Hydrol. 333, 144–154. https://doi.org/10.1016/j.jhydrol.2006.07.023.

Schär, C., Frei, C., Lüthi, D., Davies, H.C., 1996. Surrogate climate-change scenarios for regional climate models. Geophys. Res. Lett. 23 (6), 669–672. https://doi.org/10.1029/96GL00265.

Seager, R., Naik, N., Vecchi, G.A., 2010. Thermodynamic and dynamic mechanisms for large-scale changes in the hydrological cycle in response to global warming. J. Clim. 23 (17), 4651–4668. https://doi.org/10.1175/2010JCLI3655.1.

Sebastian, A., 2022. Compound flooding. In: Coastal Flood Risk Reduction. Elsevier, pp. 77–88. https://doi.org/10.1016/B978-0-323-85251-7.00007-X.

Seneviratne, S.I., Zhang, X., Adnan, M., Badi, W., Dereczynski, C., Di Luca, A., Ghosh, S., Iskandar, I., Kossin, J., Lewis, S., Otto, F., Pinto, I., Satoh, M., Vicente-Serrano, S.M., Wehner, M., Zhou, B., 2021. In: Masson-Delmotte, V., Zhai, P., Pirani, A., Connors, S. L., Péan, C., Berger, S., Caud, N., Chen, Y., Goldfarb, L., Gomis, M.I., Huang, M., Leitzell, K., Lonnoy, E., Matthews, J.B.R., Maycock, T.K., Waterfield, T., Yelekçi, O., Yu, R., Zhou, B. (Eds.), Weather and Climate Extreme Events in a Changing Climate. In Climate Change 2021: The Physical Science Basis. Contribution of Working Group I to the Sixth Assessment Report of the Intergovernmental Panel on Climate Change. Cambridge University Press, Cambridge, United Kingdom and New York, NY, USA, pp. 1513–1766. https://doi.org/10.1017/9781009157896.013.

Shi, X., Liu, Y., Chen, J., Chen, H., Wang, Y., Lu, Z., Wang, R.-Q., Fung, J.C.-H., Ng, C.W. W., 2024. Escalating tropical cyclone precipitation extremes and landslide hazards in South China under Global Warming. Npj Clim. Atmos. Sci. 7, 1–9. https://doi.org/10.1038/s41612-024-00654-w.

Simpson, R.H., Saffir, H., 1974. The hurricane disaster potential scale. Weatherwise 27 (4), 169–186. https://doi.org/10.1080/00431672.1974.9931702.

Skamarock, W.C., Klemp, J.B., Dudhia, J., Gill, D.O., Liu, Z., Berner, J., Wang, W., Powers, J.G., Duda, M.G., Barker, D.M., Huang, X.-Y., 2019. A Description of the Advanced Research WRF Model Version 4. UCAR/NCAR. https://doi.org/10.5065/1DFH-6P97.

Sun, J., He, H., Hu, X., Wang, D., Gao, C., Song, J., 2019. Numerical Simulations of Typhoon Hagupit (2008) using WRF. Weather Forecast. 34, 999–1015. https://doi.org/10.1175/WAF-D-18-0150.1.

Sun, Q., Olschewski, P., Wei, J., Tian, Z., Sun, L., Kunstmann, H., Laux, P., 2024. Key ingredients in regional climate modelling for improving the representation of typhoon tracks and intensities. Hydrol. Earth Syst. Sci. 28, 761–780. https://doi.org/10.5194/hess-28-761-2024.

Sun, Y., Yi, L., Zhong, Z., Hu, Y., Ha, Y., 2013. Dependence of model convergence on horizontal resolution and convective parameterization in simulations of a tropical cyclone at gray-zone resolutions: resolution and convection in TC simulation. J. Geophys. Res.-Atmos. 118, 7715–7732. https://doi.org/10.1002/jgrd.50606.

Swart, N.C., Cole, J.N.S., Kharin, V.V., Lazare, M., Scinocca, J.F., Gillett, N.P., Anstey, J., Arora, V., Christian, J.R., Hanna, S., Jiao, Y., Lee, W.G., Majaess, F., Saenko, O.A., Seiler, C., Seinen, C., Shao, A., Sigmond, M., Solheim, L., von Salzen, K., Yang, D., Winter, B., 2019. The Canadian Earth System Model version 5 (CanESM5.0.3). Geosci. Model Dev. 12, 4823–4873. https://doi.org/10.5194/gmd-12-4823-2019.

Tahara, R., Hiraga, Y., Kazama, S., 2025. Climate change effects on the localized heavy rainfall event in northern Japan in 2022: Uncertainties in a pseudo-global warming approach. Atmos. Res. 314, 107780. https://doi.org/10.1016/j.atmosres.2024.107780.

Tran, T.L., Ritchie, E.A., Perkins-Kirkpatrick, S.E., Bui, H., Luong, T.M., 2022. Future changes in tropical cyclone exposure and impacts in Southeast Asia from CMIP6 pseudo-global warming simulations. Earth's Future 10 (12), e2022EF003118. https://doi.org/10.1029/2022EF003118.

Tran, T.L., Ritchie, E.A., Perkins-Kirkpatrick, S.E., Bui, H., Luong, T.M., 2024. Variations in rainfall structure of Western North Pacific landfalling tropical cyclones in the warming climates. Earth's Future 12 (9), e2024EF004808. https://doi.org/10.1029/2024EF004808.

Tsuboki, K., Yoshioka, M.K., Shinoda, T., Kato, M., Kanada, S., Kitoh, A., 2015. Future increase of supertyphoon intensity associated with climate change: increase of super-typhoon intensity. Geophys. Res. Lett. 42, 646–652. https://doi.org/10.1002/2014GL061793.

Volodin, E.M., Mortikov, E.V., Kostrykin, S.V., Galin, V.Ya., Lykossov, V.N., Gritsun, A.S., Diansky, N.A., Gusev, A.V., Iakovlev, N.G., 2017. Simulation of the present-day climate with the climate model INMCM5. Clim. Dyn. 49, 3715–3734. https://doi.org/10.1007/s00382-017-3539-7.

Wang, Y., Li, H., Shi, X., Fung, J.C., 2025. Assessing the impact of cumulus convection and turbulence parameterizations on typhoon precipitation forecast. Geophysical Research Letters 52 (1), e2024GL112075. https://doi.org/10.1029/2024GL112075.

Wang, S., Toumi, R., 2022. More tropical cyclones are striking coasts with major intensities at landfall. Sci. Rep. 12, 5236. https://doi.org/10.1038/s41598-022-09287-6.

Wei, N., Song, J., Dai, Y., Jiang, S., Duan, Y., 2022. Recent decrease in inner-core rain rate of tropical cyclones over the western North Pacific. Atmos. Sci. Lett. 23 (12), e1125. https://doi.org/10.1002/asl.1125.

Xue, Z., Ullrich, P., 2021. A retrospective and prospective examination of the 1960s US northeast drought. Earth's Future 9 (7), e2020EF001930. https://doi.org/10.1029/2020EF001930.

Xue, Z., Ullrich, P.A., 2022. Sensitivity of the pseudo-global warming method under flood conditions: a case study from the Northeastern U.S.. In: Hydrometeorology/Modelling Approaches https://doi.org/10.5194/egusphere-2022-482.

Yamada, Y., Satoh, M., Sugi, M., Kodama, C., Noda, A.T., Nakano, M., Nasuno, T., 2017. Response of Tropical Cyclone activity and Structure to Global Warming in a High-Resolution Global Nonhydrostatic Model. J. Clim. 30, 9703–9724. https://doi.org/10.1175/JCLI-D-17-0068.1.

Yang, Y., Toumi, R., 2025. Large dynamic contributions to tropical cyclone precipitation with increasing sea surface temperature. Environ. Res. Lett. 20 (7), 074013. https://doi.org/10.1088/1748-9326/add753.

Yin, J., Gu, H., Liang, X., Yu, M., Sun, J., Xie, Y., Li, F., Wu, C., 2022. A possible Dynamic Mechanism for Rapid production of the Extreme Hourly Rainfall in Zhengzhou City on 20 July 2021. J. Meteorol. Res. 36, 6–25. https://doi.org/10.1007/s13351-022-1166-7.

Ying, M., Zhang, W., Yu, H., Lu, X., Feng, J., Fan, Y., Zhu, Y., Chen, D., 2014. An Overview of the China Meteorological Administration Tropical Cyclone Database. J. Atmos. Ocean. Technol. 31, 287–301. https://doi.org/10.1175/JTECH-D-12-00119.1.

Yuter, S.E., Kingsmill, D.E., Nance, L.B., Löffler-Mang, M., 2006. Observations of precipitation size and fall speed characteristics within coexisting rain and wet snow. J. Appl. Meteorol. Climatol. 45 (10), 1450–1464. https://doi.org/10.1175/JAM2406.1.

Zhang, D., Anthes, R.A., 1982. A High-Resolution Model of the Planetary Boundary Layer—Sensitivity Tests and Comparisons with SESAME-79 Data. J. Appl. Meteorol. 21, 1594–1609. https://doi.org/10.1175/1520-0450(1982)021<1594:AHRMOT>2.0.CO;2.

Zhang, Q., Liu, B., Li, S., Zhou, T., 2023. Understanding models' global sea surface temperature bias in mean state: from CMIP5 to CMIP6. Geophys. Res. Lett. 50 (4), e2022GL100888. https://doi.org/10.1029/2022GL100888.

Zhang, Y., Li, J., Liu, D., 2024. Spatial downscaling of ERA5 reanalysis air temperature data based on stacking ensemble learning. Sustainability 16 (5), 1934. https://doi.org/10.3390/su16051934.

Zhao, K., Lin, Q., Lee, W.-C., Sun, Y.Q., Zhang, F., 2016. Doppler Radar Analysis of Triple Eyewalls in Typhoon Usagi (2013). Bull. Am. Meteorol. Soc. 97, 25–30. https://doi.org/10.1175/BAMS-D-15-00029.1.